



Nonlinear dynamics of FG-GNPRC multiphase composite membranes with internal pores and dielectric properties

Zhi Ni · Yucheng Fan · Jinlong Yang · Ziyang Hang · Chuang Feng  · Jie Yang

Received: 19 March 2023 / Accepted: 9 July 2023 / Published online: 26 July 2023
© The Author(s), under exclusive licence to Springer Nature B.V. 2023

Abstract In this paper, the nonlinear dynamics of the functionally graded graphene nanoplatelet reinforced composite (FG-GNPRC) dielectric and porous membrane subjected to electro-mechanical loading is investigated. The effective material properties of multiphase composites are determined via a two-step hybrid micromechanical model. Based on the hyper-elastic membrane theory, Neo-Hookean constitutive model and the couple dielectric theory, the governing equations are obtained using an energy method considering damping and dielectric properties. Taylor series expansion (TSE) and differential quadrature (DQ) methods are utilized to discretize equations, which are then solved numerically by the incremental harmonic balance (IHB) method combined with arc-length continuation technique. The convergence analysis is carried out and the accuracy of the solution method is verified by comparing with the results of previous studies. The influence of the attributes of the internal pore, GNP, the geometric characteristics of membrane, stretching ratio and the applied electric field on forced vibration and resonance response of the system are analyzed.

Keywords Nonlinear dynamics · Graphene nanoplatelet · Porous membrane · Dielectric properties

1 Introduction

Thin dielectric elastomer membranes with compliant electrodes have been found to be highly useful in a variety of applications, such as actuators [1, 2], sensors [3, 4], energy harvesting [5, 6], soft robotics [7, 8], etc. These elastomers are primarily attractive due to their uncomplicated working mechanism, whereby the application of electric field results in the expansion of the membrane due to the bulk incompressibility of the elastomer and Coulomb force between the electrodes. This interaction between constitutive and geometric nonlinearities leads to a complex behavior in thin dielectric membrane. In addition to dynamics, their energy efficiency and scale-production with moderate cost have made them a promising material candidate for mass production. Pores are usually introduced into the material during the preparation and manufacturing process, and their presence can have a significant impact on the dynamic performance of the structure [9–11]. Meanwhile, the dielectric permittivity of the dielectric elastomer membrane is relatively small, which restricts its use in broader engineering fields.

To overcome the limitations mentioned above, it has been shown that adding additives can improve the

Z. Ni · Y. Fan · J. Yang · Z. Hang · C. Feng (✉)
College of Civil Engineering, Nanjing Tech University,
Nanjing 211816, China
e-mail: chuang.feng@njtech.edu.cn

J. Yang
School of Engineering, RMIT University,
Melbourne 3083, Australia

mechanical and dielectric properties. Among the suggested additives, graphene nanoplatelet (GNP) has been found to be one of the most effective one, as it greatly enhances the mechanical and dielectric properties without significantly increasing the weight of the structure. In regard of mechanical enhancement, the experiments conducted by Wang et al. [12] demonstrated that the tensile strength of composites was significantly increased when GNP was added. By utilizing atomic modeling techniques, Sun et al. [13] discovered a considerable enhancement in the elastic properties of GNP reinforced composites. Mahmum et al. [14] further explored the elastic properties of GNP reinforced nanocomposites with various analytical models and found that the Young's modulus of the composites had increased significantly. Research also shows that GNP reinforced composites can significantly improve the electrical properties of the composites. Mergen et al. [15] investigated the dielectric relaxation properties and AC conductivity of nanocomposites. The results indicated that the incorporation of GNP fillers significantly increased the capacitive/charge storage capabilities of the nanocomposites. Liu et al. [16] created a composite of GNP/polyvinylidene fluoride (PVDF) and discovered that GNP significantly increased the dielectric constant of the composite because of the increased polarization. The model of Xia et al. [17] also demonstrated the enhanced dielectric properties of polymer nanocomposites reinforced with GNP.

Furthermore, to maximize the effectiveness and efficiency of graphene fillers, the concept of functionally graded graphene nanoplatelet reinforced composite (FG-GNPRC) has been proposed. Research on the analysis of FG-GNPRC materials and structures has been conducted by numerous papers. Feng et al. [18, 19] performed the investigation on the geometrically nonlinear free vibration and the nonlinear bending of FG-GNPRC beams. The research conducted by Shen et al. [20] focused on the nonlinear vibration of FG-GNPRC beams subjected to thermal environments by utilizing a two-step perturbation approach. Song et al. [21, 22] used a differential quadrature method to analyze free vibration and buckling of cracked FG-GNPRC beams resting on an elastic foundation. Li et al. [23] studied the nonlinear primary and secondary resonances of the FG-GNPRC beams based upon the third-order shear deformation theory. By the implementation of Ritz

method, Song et al. [24] investigated nonlinear dynamic instability of edge-cracked FG-GNPRC beams within the framework of first-order shear deformation theory. The study conducted by Wang et al. [25] revealed that the nonlinear vibration of the FG-GNPRC plate can be actively adjusted by altering the characteristics of the electrical fields. Song et al. [26] introduced a modified nonlinear Hertz contact theory for analyzing low-velocity impact response of FG-GNPRC plate based on the first-order shear deformation plate theory and von Kármán-type nonlinear kinematics. Dong et al. [27] employed the Galerkin technique to explore the effects of various material and geometry parameters on the vibration behavior of FG cylindrical shells. Ye et al. [28] analyzed nonlinear forced vibration of FG-GNPRC metal foam cylindrical shells via the pseudo-arclength continuation technique.

Despite numerous studies focusing on examining the geometric and material characteristics of FG-GNPRC beams, plates, and shells, few investigations have centered on the nonlinear dynamic response of FG-GNPRC membrane structures, particularly with regards to the dielectric properties of the composites. The internal pores of these structures have been identified as having a crucial impact on their behavior, yet previous studies have either neglected this aspect or relied on empirical formulas to approximate their influence. Consequently, a two-step hybrid micromechanical model is presented to investigate the nonlinear dynamic response of the FG-GNPRC membrane. The objective of this methodology is to acquire a deeper insight into the structural performance of porous composite membranes.

To fill research gap, this paper investigates the damped nonlinear dynamics of the dielectric membrane involving the effect of pore. The proposed structure is a GNPRC dielectric membrane, assumed to be circular with axisymmetric geometrical and physical properties, as shown in Fig. 1, with a fixed boundary condition applied around the membrane. The compliant electrodes are placed on two faces and connected to an external voltage, and a harmonic base excitation is applied transversely to the membrane. Effective medium theory (EMT), Mori–Tanaka (MT) model and rule of mixture are utilized to evaluate the effective material properties of the composite membrane. Hamilton's principle is applied to derive the governing equations for the nonlinear damped

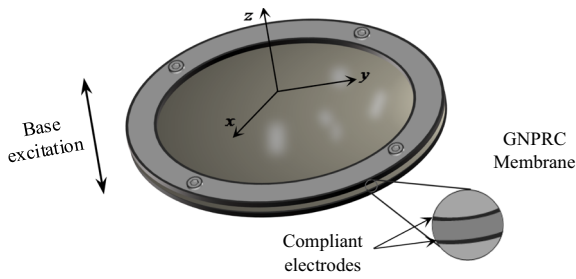


Fig. 1 GNPRC membrane with electric and base excitations

vibration based on hyperelastic membrane theory, Neo-Hookean constitutive model and the couple dielectric theory. With the aid of Taylor series expansion (TSE) and differential quadrature (DQ) methods, the governing equations are discretized, followed by numerical solution using the incremental harmonic balance (IHB) method combined with the arc-length algorithm. A comprehensive parametric study is conducted to gain a deeper understanding of the intrinsic complexity of this dynamic system.

2 Determination of material properties

To achieve functionally graded structures, apart from uniform dispersion (profile U), four functionally graded distributions, i.e. profiles X, O, A and V, are involved in present study (as shown in Fig. 2). In Profile U, the GNP content keeps the same throughout the thickness while the concentration of GNP reinforcements linearly increases and decreases from the midplane to top and bottom surfaces of the membrane in profiles X and O, respectively. For profile A and V, the GNP content increases and decreases uniformly

from the top to the bottom of the membrane, respectively. The volume fraction of the multi-layer structure in the thickness direction of the membrane is

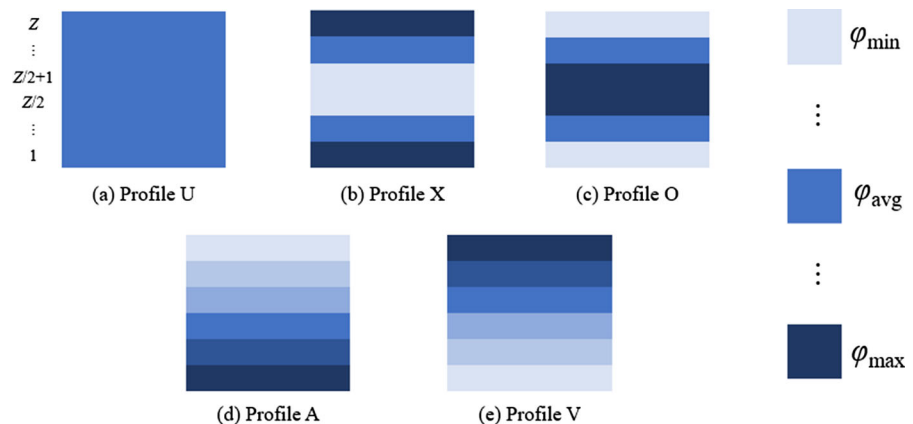
$$\begin{aligned}
 U : \varphi_{(i)} &= \varphi_{\text{avg}} \\
 X : \varphi_{(i)} &= \frac{Z - 2 - (Z - 2|Z + 1 - 2i|)S_g}{Z - 2} \varphi_{\text{avg}} \\
 O : \varphi_{(i)} &= \frac{Z - 2 + (Z - 2|Z + 1 - 2i|)S_g}{Z - 2} \varphi_{\text{avg}} \quad (1) \\
 A : \varphi_{(i)} &= \frac{Z - 1 + (2i - Z - 1)S_g}{Z - 1} \varphi_{\text{avg}} \\
 V : \varphi_{(i)} &= \frac{Z - 1 - (2i - Z - 1)S_g}{Z - 1} \varphi_{\text{avg}}
 \end{aligned}$$

where $\varphi_{(i)}$ denotes the GNP volume fraction of the i th layer of the composite membrane. The average volume fraction of GNP is represented by φ_{avg} . The variation of GNP components is expressed by the slope factor S_g , which is calculated as $(\varphi_{\text{max}} - \varphi_{\text{min}}) / (\varphi_{\text{max}} + \varphi_{\text{min}})$, where φ_{max} and φ_{min} are the maximum and minimum GNP concentration in the layers, respectively. The number of layers is represented by Z . It should be noted that the GNP volume fraction can be calculated using the GNP weight fraction f_{GNP} and the densities of the GNP and matrix [29].

2.1 Hybrid micromechanical model

Considering the internal pores, GNPRC transforms from a two-phase material into a multi-phase composite, which makes it difficult to apply traditional micromechanical models to determine its material properties. To address this challenge, a two-step hybrid micromechanical model is developed in this study, and the accuracy of its prediction of mechanical

Fig. 2 GNP distribution profiles **a** Profile U; **b** Profile X; **c** Profile O; **d** Profile A; **e** Profile V



and electrical properties of multiphase composite has been verified [30]. The approach involves treating both GNP and the pores as reinforcing fillers in two separate steps. The homogenization process for determining the mechanical and electrical properties of GNPRC with pores is outlined as follows: Firstly, GNP serves as the reinforcing filler while EMT is utilized to homogenize GNPRC without considering the pores. Then, in the second homogenization process, GNPRC is treated as the matrix and the pores are regarded as reinforcing fillers. This process is illustrated in Fig. 3.

The effectiveness of EMT in predicting the mechanical and electrical properties of GNPRC has been established, thereby enabling the determination of the material properties of GNPRC as a two-phase composite, without considering internal pores [17, 31], i.e.

$$\begin{aligned} & (1 - \varphi_{(i)}) \frac{L_m - L_e}{L_m + (1/3)(L_m - L_e)} \\ & + \frac{1}{3} \varphi_{(i)} \sum_{k=1}^3 \frac{L_k - L_e}{L_e + S_{kk}(L_k - L_e)} = 0 \quad (k = 1, 2, 3) \end{aligned} \tag{2}$$

where φ and L denotes the volume fraction and moduli tensor, respectively. The subscript “m” and “e” refer to the matrix and effective medium, respectively. The k th component of the filler’s Eshelby tensor is designated by S_{kk} . Considering the GNP reinforcement as a thin oblate spheroid, the following applies [32, 33]

$$\begin{aligned} S_{11} = S_{22} &= \frac{\alpha}{2(1 - \alpha^2)^{3/2}} \left[\arccos \alpha - \alpha(1 - \alpha^2)^{1/2} \right] \\ S_{33} &= 1 - 2S_{11} \end{aligned} \tag{3}$$

where α is calculated as the ratio of t_{GNP} (the thickness of the GNP) to D_{GNP} (the diameter of the GNP).

For determining the electrical properties of the GNPRC, Eq. (2) can be converted into

$$\begin{aligned} & (1 - \varphi_{(i)}) \frac{\sigma_m^* - \sigma_e^*}{\sigma_e^* + (1/3)(\sigma_m^* - \sigma_e^*)} \\ & + \frac{1}{3} \varphi_{(i)} \sum_{k=1}^3 \frac{\sigma_k^* - \sigma_e^*}{\sigma_e^* + S_{kk}(\sigma_k^* - \sigma_e^*)} \\ & = 0 \end{aligned} \tag{4}$$

where σ_m^* , σ_k^* and σ_e^* are the complex conductivity of the matrix, the k th component of the fillers and the composite, respectively. The parameter σ^* which denotes complex electrical conductivity can be expressed as $\sigma^* = \sigma + i2\pi f_{\text{AC}}\varepsilon$, where σ and ε represent electrical conductivity and dielectric permittivity of the composites, respectively, and f_{AC} refers to the frequency of the alternating current (AC) electrical field in Hertz.

An interphase layer is typically introduced around the reinforcing fillers to address the imperfect bonding or interaction between the filler and matrix, resulting in modifications to the electrical conductivity and dielectric permittivity of the fillers [17]

$$\begin{cases} \sigma_k^{(c)} = \sigma_0^{(int)} \left[1 + \frac{(1 - \varphi_{int})(\sigma_k - \sigma_0^{(int)})}{\varphi_{int}S_{kk}(\sigma_k - \sigma_0^{(int)}) + \sigma_0^{(int)}} \right] \\ \varepsilon_k^{(c)} = \varepsilon_0^{(int)} \left[1 + \frac{(1 - \varphi_{int})(\varepsilon_k - \varepsilon_0^{(int)})}{\varphi_{int}S_{kk}(\varepsilon_k - \varepsilon_0^{(int)}) + \varepsilon_0^{(int)}} \right] \end{cases} \quad (k = 1, 2, 3) \tag{5}$$

where $\sigma_0^{(int)}$ and $\varepsilon_0^{(int)}$ denote the conductivity and dielectric permittivity of the interphase, respectively,

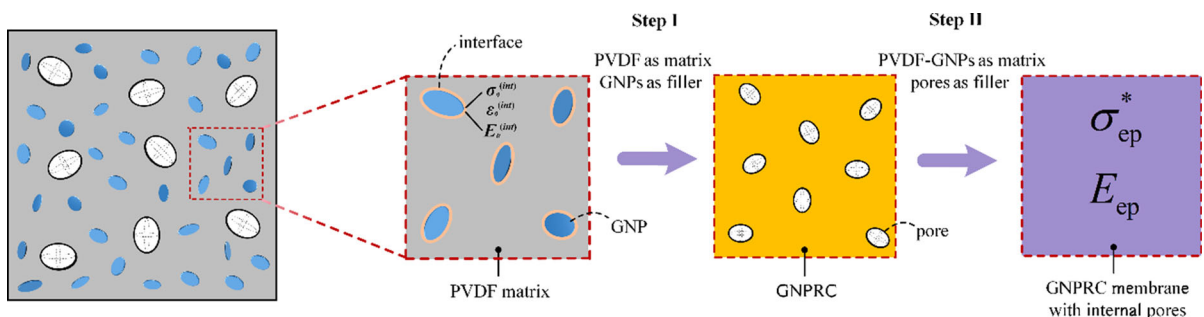


Fig. 3 Two-step method for determining effective properties of GNPRC membrane with internal pores

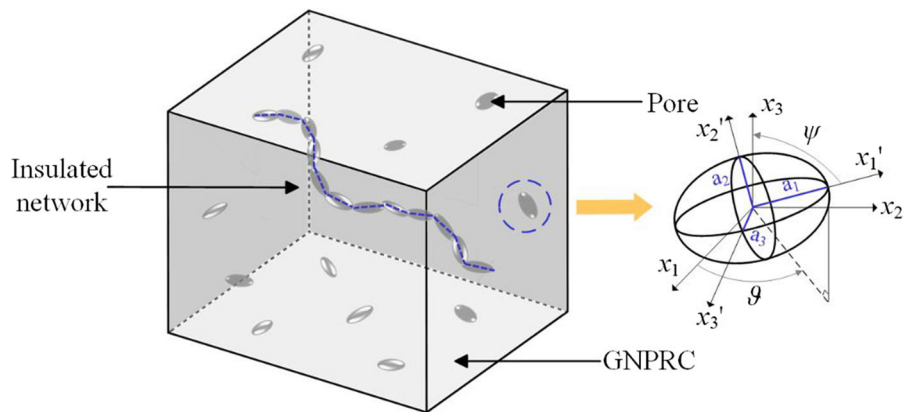


Fig. 4 Representative volume element (RVE) of composites containing pores

and φ_{int} denotes the volume fraction of the surrounding interphase.

While evaluating the electrical conductivity of graphene fillers with interfacial phase, it is necessary to integrate the effect of electron tunneling. When determining the dielectric permittivity, the impact of Maxwell–Wagner–Sillars (MWS) polarization should also be considered [17, 31–34]. In order to incorporate the above effects, the conductivity and dielectric permittivity in Eq. (5) can be further modified as described in [17, 34–37].

For mechanical properties of the GNPRC, Eq. (2) can be transformed into

$$\begin{aligned} & (1 - \varphi_{(i)}) \frac{E_m - E_e}{E_m + (1/3)(E_m - E_e)} \\ & + \frac{1}{3} \varphi_{(i)} \sum_{k=1}^3 \frac{E_k - E_e}{E_e + S_{kk}(E_k - E_e)} \\ & = 0 \end{aligned} \tag{6}$$

where E_m is the elastic modulus of the matrix, E_k is the elastic modulus of the reinforcing filler in the k th direction and E_e is the effective elastic modulus of the composites. Similar to electrical properties, when considering the interphase surrounding the GNP, the effective elastic modulus is altered as

$$E_k^{(c)} = E_0^{(int)} \left[1 + \frac{(1 - \varphi_{int})(E_k - E_0^{(int)})}{\varphi_{int} S_{kk}(E_k - E_0^{(int)}) + E_0^{(int)}} \right] \tag{7}$$

$(k = 1, 2, 3)$

where $E_0^{(int)}$ represents the elastic modulus of the interphase surrounding GNP.

In the present study, ellipsoid-shaped hollow fillers dispersed in GNPRC are treated as pores whose presence, as reported in previous studies [10, 38], can affect the electrical and mechanical properties of the composite membrane by forming insulated networks that impact the transport of electrical carriers. In Fig. 4, the orientation of the pores in the local coordinate system is denoted by two Euler angles, ψ and ϑ . The ellipsoid pores have an aspect ratio, α_p , defined as a_2/a_1 , where a_1 and a_2 are respectively the half lengths of the principal axes along x_1' and x_2' . n is porosity which denotes the volume fraction of the pores.

Mori–Tanaka (MT) model [39] is utilized to determine the electrical properties of the porous composites, the effective complex electrical conductivity σ_{ep}^* is expressed as

$$\begin{aligned} \sigma_{ep}^* &= \sigma_e^* \\ &+ n \frac{\int_0^{2\pi} \int_0^\pi ODF(\psi, \vartheta) (\sigma_p^* - \sigma_e^*) G \sin \vartheta d\vartheta d\psi}{\int_0^{2\pi} \int_0^\pi ODF(\psi, \vartheta) G \sin \vartheta d\vartheta d\psi} \end{aligned} \tag{8}$$

where σ_p^* denotes the complex electrical conductivity of pores filled with air. The orientation distribution function (ODF), which describes the distribution of ellipsoidal pores in the matrix and is equal to unity for a completely random distribution, is denoted by $ODF(\psi, \vartheta)$. The electric field concentration tensor G can be obtained through the MT model [39].

Considering the overall mechanical properties of the porous composites, the effective elastic modulus E_{ep} can be expressed as [40]

$$E_{ep} = E_c + n \frac{\int_0^{2\pi} \int_0^\pi ODF(\psi, \vartheta) (E_p - E_c) G \sin \vartheta d\vartheta d\psi}{\int_0^{2\pi} \int_0^\pi ODF(\psi, \vartheta) G \sin \vartheta d\vartheta d\psi} \tag{9}$$

where E_p denotes the elastic modulus of pores.

2.2 Rule of mixture

The rule of mixture is used to determine the Poisson’s ratio $\nu_{(i)}$ and density $\gamma_{(i)}$ of the i th layer

$$\begin{cases} \nu_{(i)} = (1 - \varphi_{(i)} - \varphi_{p(i)})\nu_m + \varphi_{(i)}\nu_{GNP} + \varphi_{p(i)}\nu_p \\ \gamma_{(i)} = (1 - \varphi_{(i)} - \varphi_{p(i)})\gamma_m + \varphi_{(i)}\gamma_{GNP} + \varphi_{p(i)}\gamma_p \end{cases} \tag{10}$$

where subscript “m”, “GNP” and “p” represent the matrix, the GNP filler and pore, respectively.

3 Governing equations

3.1 Analytical modelling

Pre-stretch technology is often used in membrane structures to prevent pull-in between electrodes [41]. Figure 5 exhibits the three configurations of the membrane before and after pre-stretch and deformation out of the plane. The radial pre-stretch applied at the initial state causes the membrane’s radius changing from b to B , correspondingly, the point M_1 moves to M_2 . Then the membrane undergoes the out-of-plane deformation induced by the base excitation and electrical loading, M_2 further moves to M_3 . Using spherical coordinates, the positions of the three points are

$$M_1 = (\rho, \theta, 0), M_2 = (r_0, \theta, 0), M_3 = (r, \theta, z) \tag{11}$$

where r denotes the radius of the projection of M_3 in the planar and z denotes the distance of M_3 from the xoy plane. They can be expressed as

$$\begin{cases} r(\rho, t) = r_0(\rho) + u(\rho, t) = \eta\rho + u(\rho, t) \\ z(\rho, t) = z_0(\rho) + w(\rho, t) = w(\rho, t) \end{cases} \tag{12}$$

where u and w respectively represent the radial and transverse displacements of the point M_2 after out-of-plane deformation, and the stretching ratio η is defined as $\eta = B/b$.

As depicted in Fig. 5, the three principal stretches can be written as

$$\mu_i = \frac{dS_i}{ds_i} \quad (i = 1, 2, 3) \tag{13}$$

where dS_i and ds_i are the undeformed and deformed length of an infinitesimal element in the principal direction, respectively. The subscripts “1”, “2” and “3” correspond to the meridional, circumferential, and transverse directions, respectively.

The differential is defined as $\partial(\cdot)/\partial t = (\cdot)_{,t}$, $\partial(\cdot)/\partial \rho = (\cdot)_{,\rho}$, $\partial^2(\cdot)/\partial t^2 = (\cdot)_{,tt}$, $\partial^2(\cdot)/\partial \rho^2 = (\cdot)_{,\rho\rho}$. The lengths in the meridional and circumferential directions can be expressed as

$$\begin{cases} \mu_1 = \sqrt{(r_\rho)^2 + (z_\rho)^2} \\ \mu_2 = \frac{r}{\rho} \end{cases} \tag{14}$$

With the assumption of material incompressibility, the principal stretch μ_3 is expressed as

$$\mu_3 = \frac{H}{h} = \frac{1}{\mu_1\mu_2} = \frac{\rho}{r\sqrt{(r_\rho)^2 + (z_\rho)^2}} \tag{15}$$

where h and H are the thickness of the membrane before and after deformation, respectively.

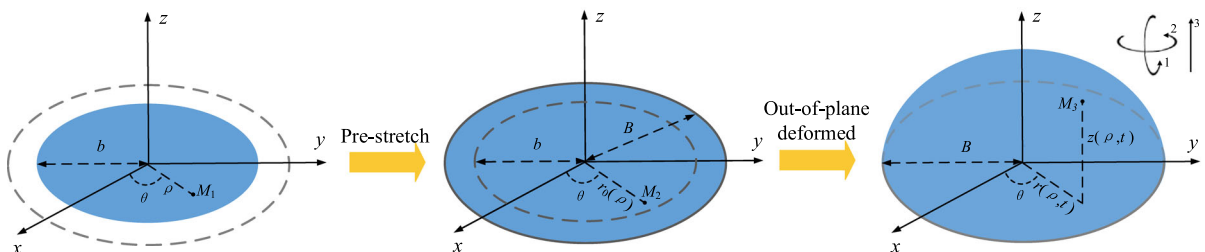


Fig. 5 Sequence of deformation for an axisymmetric circular membrane

3.2 Theoretical framework

Neo-Hookean model [42] is used to characterize the hyperelastic response of the membrane, the first strain invariant I_1 is given by

$$\begin{aligned}
 I_1 &= \sum_{i=1}^3 \mu_i^2 = \mu_1^2 + \mu_2^2 + \mu_3^2 \\
 &= (r_\rho)^2 + (z_\rho)^2 + \frac{r^2}{\rho^2} + \frac{\rho^2}{r^2 [(r_\rho)^2 + (z_\rho)^2]} \quad (16)
 \end{aligned}$$

The mechanical behavior of the materials can be described via the strain density function [43–46], i.e.

$$\begin{aligned}
 W_{1(i)} &= C_{1(i)}(I_1 - 3) \\
 &= C_{1(i)} \left\{ (r_\rho)^2 + (z_\rho)^2 + \frac{r^2}{\rho^2} + \frac{\rho^2}{r^2 [(r_\rho)^2 + (z_\rho)^2]} - 3 \right\} \quad (17)
 \end{aligned}$$

where $C_{1(i)}$ denotes a parameter related to the linear shear modulus of i th layer.

Assuming the material is homogeneous and isotropic, the electric displacement vector $\mathbf{D}_{(i)}$ of the i th layer in the transverse direction can be expressed as

$$\mathbf{D}_{(i)} = \varepsilon_{r(i)} \varepsilon_0 \mathbf{E}_{(i)} \quad (18)$$

where $\varepsilon_{r(i)}$ and ε_0 are respectively the relative permittivity of the i th layer of the membrane material and the vacuum. The electric field component, $E_{(i)}$, within the i th layer of the membrane can be determined by the voltage, $V_{(i)}$, across the membrane’s electrode, i.e.

$$E_{(i)} = \frac{V_{(i)}}{H} = \frac{V_{(i)} \mu_1 \mu_2}{h} \quad (19)$$

Considering electrical polarization of the continuum [47], the electrostatic energy per unit volume of the i th layer resulting from the dielectric properties of the composites are expressed as

$$W_{b(i)} = \frac{\mathbf{D}_{(i)}^2}{2\varepsilon_{r(i)}\varepsilon_0} = \frac{\varepsilon_{r(i)}\varepsilon_0 E_{(i)}^2}{2} \quad (20)$$

Then the Helmholtz free energy of the i th layer of the composites per unit volume is given by [47]

$$\begin{aligned}
 W_{a(i)} &= W_{1(i)}(\mu_1 + \mu_2 + \mu_3) + W_{b(i)} \\
 &= W_{1(i)}(\mu_1 + \mu_2 + \mu_3) + \frac{\varepsilon_{r(i)}\varepsilon_0 E_{(i)}^2}{2} \quad (21)
 \end{aligned}$$

The total electrostatic energy $W_{b(all)}$ of the composite membrane can be written as

$$W_{b(all)} = \sum_{i=1}^{N_L} \int_{h_i}^{h_{i+1}} W_{b(i)} dz = \frac{1}{2} \sum_{i=1}^{N_L} \int_{h_i}^{h_{i+1}} \varepsilon_{r(i)} \varepsilon_0 E_{(i)}^2 dz \quad (22)$$

Equation (21) can also be derived from the composite membrane’s equivalent permittivity [48], i.e.

$$W_{b(all)} = \frac{1}{2} \varepsilon_0 \int_{-\frac{h}{2}}^{\frac{h}{2}} \varepsilon_{(all)} E_{(i)}^2 dz \quad (23)$$

where $\varepsilon_{(all)}$ is the overall equivalent permittivity of the material, given as

$$\varepsilon_{(all)} = \frac{N_L}{\sum_{i=1}^{N_L} \frac{1}{\varepsilon_{r(i)}}} \quad (24)$$

3.3 Energy integrals

To derive the governing equations, Hamilton’s principle can be employed, i.e.

$$\delta \int_{t_1}^{t_2} (T_e - U_e + W_e) dt = 0 \quad (25)$$

where T_e is the kinetic energy, U_e is the potential energy and W_e is the work done by the radial force f_r and damping force F_r . The variational form of the three energies are expressed as [49]

$$\begin{aligned}
 \delta \int_{t_1}^{t_2} T_e dt &= \frac{1}{2} \delta \sum_{i=1}^{N_L} \int_{t_1}^{t_2} \int_{h_i}^{h_{i+1}} \int_0^{2\pi} \int_0^b \gamma_{(i)} (r_r^2 + z_r^2) \rho d\rho d\theta dz dt \\
 &= 2\pi \sum_{i=1}^{N_L} \int_{t_1}^{t_2} \int_{h_i}^{h_{i+1}} \int_0^b \gamma_{(i)} (r_r \delta r_r + z_r \delta z_r) \rho d\rho dz dt \\
 &= 2\pi \sum_{i=1}^{N_L} \int_{t_1}^{t_2} \int_{h_i}^{h_{i+1}} \int_0^b \gamma_{(i)} r_r \rho d\rho dz d(\delta r) \\
 &\quad + 2\pi \sum_{i=1}^{N_L} \int_{t_1}^{t_2} \int_{h_i}^{h_{i+1}} \int_0^b \gamma_{(i)} z_r \rho d\rho dz d(\delta z) \quad (26) \\
 &= r_r \delta r \Big|_{t_1}^{t_2} - 2\pi \sum_{i=1}^{N_L} \int_{h_i}^{h_{i+1}} \int_0^b \gamma_{(i)} (r_n \delta r) \rho d\rho dz \\
 &\quad + z_r \delta z \Big|_{t_1}^{t_2} - 2\pi \sum_{i=1}^{N_L} \int_{h_i}^{h_{i+1}} \int_0^b \gamma_{(i)} (z_n \delta z) \rho d\rho dz \\
 &= -2\pi \sum_{i=1}^{N_L} \int_{h_i}^{h_{i+1}} \int_0^b \gamma_{(i)} (r_n \delta r + z_n \delta z) \rho d\rho dz
 \end{aligned}$$

and

$$\begin{aligned}
\delta \int_{t_1}^{t_2} U_e dt &= \delta \sum_{i=1}^{N_L} \int_{t_1}^{t_2} \int_{h_i}^{h_{i+1}} \int_0^{2\pi} \int_0^b W_{a(i)} \rho d\rho d\theta dz dt \\
&= 2\pi \sum_{i=1}^{N_L} \int_{t_1}^{t_2} \int_{h_i}^{h_{i+1}} \int_0^b \delta W_{a(i)} \rho d\rho dz dt \\
&= 2\pi \sum_{i=1}^{N_L} \int_{t_1}^{t_2} \int_{h_i}^{h_{i+1}} \int_0^b [W_{a(i)r} \delta r + W_{a(i)r\rho} \delta r_\rho + W_{a(i)z\rho} \delta z_\rho] \rho d\rho dz dt \\
&= 4\pi \sum_{i=1}^{N_L} \int_{t_1}^{t_2} \int_{h_i}^{h_{i+1}} \int_0^b C_{1(i)} \left\{ \frac{r \delta r}{\rho^2} - \rho^2 \frac{r_\rho \delta r_\rho + z_\rho \delta z_\rho}{r^2 [(r_\rho)^2 + (z_\rho)^2]^2} - \frac{\rho^2 \delta r}{r^3 [(r_\rho)^2 + (z_\rho)^2]} \right\} \rho d\rho dz dt \\
&\quad + 2\pi \sum_{i=1}^{N_L} \int_{t_1}^{t_2} \int_{h_i}^{h_{i+1}} \int_0^b \left\{ 2C_{1(i)} (r_\rho \delta r_\rho + z_\rho \delta z_\rho) + r^2 \frac{\varepsilon_0 \varepsilon_r(i) V_{(i)}^2}{h^2 \rho^2} [(r_\rho)^2 + (z_\rho)^2]^2 \right\} \rho d\rho dz dt
\end{aligned} \tag{27}$$

$$\begin{aligned}
\delta \int_{t_1}^{t_2} W_e dt &= \delta f_r (r - \rho) |_{\rho=b} \\
&\quad + 2\pi \sum_{i=1}^{N_L} \int_{t_1}^{t_2} \int_{h_i}^{h_{i+1}} \int_0^b (-c_1 r_t \delta r - c_2 z_t \delta z) \rho d\rho dz dt
\end{aligned} \tag{28}$$

where c_1 and c_2 are the viscous damping coefficient.

Substituting Eq. (12) into Eqs. (26)–(28) and adding a base excitation term to the transverse motion, denoted by $p(t)$, the governing equations for FG-GNPRC membrane can be obtained as

$$\begin{aligned}
&\sum_{i=1}^{N_L} \int_{h_i}^{h_{i+1}} (\gamma_{(i)} u_{tt} + c_1 u_t) dz \\
&\quad - 2 \sum_{i=1}^{N_L} \int_{h_i}^{h_{i+1}} C_{1(i)} \left(\frac{1}{\rho} u_\rho + u_{\rho\rho} - \frac{u}{\rho^2} + \frac{A_2}{A_1} \right) dz \\
&\quad + \sum_{i=1}^{N_L} \int_{h_i}^{h_{i+1}} \frac{\varepsilon_0 \varepsilon_r(i) V_{(i)}^2}{h^2 \rho^2} \left[u (w_\rho)^2 + \frac{u^2}{\rho} u_\rho - u (u_\rho)^2 - u^2 u_{\rho\rho} \right] dz \\
&\quad + \sum_{i=1}^{N_L} \int_{h_i}^{h_{i+1}} \frac{\varepsilon_0 \varepsilon_r(i) V_{(i)}^2}{h^2 \rho^2} \left\{ \eta^2 (u - \rho^2 u_{\rho\rho} - \rho u_\rho) \right. \\
&\quad \left. + \eta \left[\frac{u^2}{\rho} + \rho (w_\rho)^2 - \rho (u_\rho)^2 - \rho^2 u u_{\rho\rho} \right] \right\} dz = 0
\end{aligned} \tag{29}$$

and

$$\begin{aligned}
&\sum_{i=1}^{N_L} \int_{h_i}^{h_{i+1}} (\gamma_{(i)} w_{tt} + p + c_2 w_t) dz - 2 \sum_{i=1}^{N_L} \int_{h_i}^{h_{i+1}} \\
&\quad C_{1(i)} \left(\frac{1}{\rho} w_\rho + w_{\rho\rho} + \frac{A_3}{A_1} \right) dz \\
&\quad - \sum_{i=1}^{N_L} \int_{h_i}^{h_{i+1}} \frac{\varepsilon_0 \varepsilon_r(i) V_{(i)}^2}{h^2 \rho^2} \left(2\eta u_\rho w_\rho + \frac{2u}{\rho} u_\rho w_\rho + 2\eta u w_{\rho\rho} \right. \\
&\quad \left. - \frac{u^2}{\rho^2} w_\rho + \frac{u^2}{\rho} w_{\rho\rho} + \eta^2 \rho w_{\rho\rho} + \eta^2 w_\rho \right) dz = 0
\end{aligned} \tag{30}$$

where the terms A_1 , A_2 and A_3 are given in the Appendix 1.

A clamped boundary condition is supposed to be applied around the membrane, i.e.

$$\begin{cases} u(0, t) = r(0, t) = 0 \\ w(b, t) = z(b, t) = 0 \\ r(b, t) = \eta b \\ u(b, t) = 0 \end{cases} \tag{31}$$

For the above coupled strongly nonlinear governing equations, Eqs. (29) and (30) can be discretized directly by using the DQ method poses a challenge. To address this, TSE approach is utilized, i.e.

$$\left\{ \begin{aligned} & -\frac{\psi_1}{\rho^2}u + \frac{\psi_1}{\rho}u_\rho + \psi_1u_{\rho\rho} + \frac{3\eta\lambda_1 - \eta\lambda_2}{\rho^3}u^2 - \frac{6\lambda_1}{\rho^4}u^3 - \frac{2\eta(\lambda_1 - \lambda_2)}{\rho}uu_{\rho\rho} - \frac{3\eta\lambda_1 - \eta\lambda_2}{\rho}(u_\rho)^2 \\ & + \frac{6\lambda_1}{\rho}(u_\rho)^3 - \frac{3\lambda_1 + \lambda_2}{\rho^3}u^2u_\rho + \frac{3\lambda_1 + \lambda_2}{\rho^2}u^2u_{\rho\rho} + \frac{3\lambda_1 + \lambda_2}{\rho^2}u(u_\rho)^2 + \frac{\eta}{\rho}\left(\frac{\lambda_1}{3} - \lambda_2\right)(w_\rho)^2 \\ & + \frac{\lambda_1 - \lambda_2}{\rho^2}u(w_\rho)^2 - \frac{8\lambda_1}{3\rho}uw_\rho w_{\rho\rho} + \frac{8\lambda_1}{\rho}uu_\rho u_{\rho\rho} - \frac{10\lambda_1}{3\rho}u_\rho(w_\rho)^2 + A_4 = \sum_{i=1}^{N_L} \int_{h_i}^{h_{i+1}} [\gamma_{(i)}u_{tt} + c_1u_t] dz \\ & \frac{\psi_2}{\rho}w_\rho + \psi_2w_{\rho\rho} + \frac{2\eta(\lambda_1 + \lambda_2)}{\rho}u_\rho w_\rho + \left(\frac{4\eta\lambda_1}{3\rho} + \frac{2\eta\lambda_2}{\rho}\right)uw_{\rho\rho} - \frac{(\lambda_1 - \lambda_2)}{\rho^2}(2uu_\rho w_\rho + u^2w_{\rho\rho}) + A_5 \\ & + \frac{(\lambda_1 - \lambda_2)}{\rho^3}u^2w_\rho - \frac{\lambda_1}{\rho}\left[6w_\rho(u_\rho)^2 + \frac{8u}{3}w_\rho u_{\rho\rho} + \frac{8u}{3}u_\rho w_{\rho\rho} - \frac{2}{3}(w_\rho)^3\right] = \sum_{i=1}^{N_L} \int_{h_i}^{h_{i+1}} [\gamma_{(i)}w_{tt} + p + c_2w_t] dz \end{aligned} \right. \tag{32}$$

where A_4 and A_5 in Eq. (32) are given in the Appendix

1. $\lambda_1, \lambda_2, \psi_1,$ and ψ_2 as involved are

$$\left\{ \begin{aligned} \lambda_1 &= \frac{6}{\eta^8} \sum_{i=1}^{N_L} \int_{h_i}^{h_{i+1}} C_{1(i)} dz \\ \lambda_2 &= \sum_{i=1}^{N_L} \int_{h_i}^{h_{i+1}} \frac{V_{(i)}^2 \varepsilon_0 \varepsilon_r(i)}{h^2} dz \\ \psi_1 &= \sum_{i=1}^{N_L} \int_{h_i}^{h_{i+1}} \left[2C_{1(i)} \left(1 + \frac{3}{\eta^6} \right) + \eta^2 \frac{V_{(i)}^2 \varepsilon_0 \varepsilon_r(i)}{h^2} \right] dz \\ \psi_2 &= \sum_{i=1}^{N_L} \int_{h_i}^{h_{i+1}} \left[2C_{1(i)} \left(1 - \frac{1}{\eta^6} \right) + \eta^2 \frac{V_{(i)}^2 \varepsilon_0 \varepsilon_r(i)}{h^2} \right] dz \end{aligned} \right. \tag{33}$$

It should be mentioned that the parameter h gives rise to the nonlinearity in the system.

4 Solution

The following quantities are introduced to normalize the governing equations

$$\begin{aligned} U &= \frac{u}{h}, W = \frac{w}{h}, \chi = \frac{\rho}{b}, \tau = \frac{t}{b} \sqrt{\frac{C_0}{\gamma_0}}, \kappa = \frac{h}{b}, \gamma_{1(i)} = \frac{\gamma_{(i)}}{\gamma_0}, C_{10(i)} = \frac{C_{1(i)}}{C_0} \\ c_{10} &= \frac{c_1 b}{\sqrt{\gamma_0 C_0}}, c_{20} = \frac{c_2 b}{\sqrt{\gamma_0 C_0}}, P = \frac{p}{\kappa C_0 P} \end{aligned} \tag{34}$$

where γ_0 and C_0 represent the corresponding values of the matrix, respectively. Substituting Eq. (34) into Eq. (32) and defining $\partial(\cdot)/\partial\tau = (\cdot)_\tau, \partial(\cdot)/\partial\chi = (\cdot)_\chi, \partial^2(\cdot)/\partial\tau^2 = (\cdot)_{\tau\tau}$ and $\partial^2(\cdot)/\partial\chi^2 = (\cdot)_{\chi\chi}$, the dimensionless governing equations are obtained, i.e.

$$\left\{ \begin{aligned} & 2a_1 \left(1 + \frac{3}{\eta^6} \right) \left(-\frac{1}{\chi^2}U + \frac{1}{\chi}U_\chi + U_{\chi\chi} \right) + \frac{6a_1}{\eta^7} \kappa \left[\frac{4}{3}W_\chi W_{\chi\chi} + \frac{3}{\chi^3}U^2 + \frac{11}{3\chi}(W_\chi)^2 \right. \\ & \left. - \frac{2}{\chi}UU_{\chi\chi} - 4U_\chi U_{\chi\chi} - \frac{3}{\chi}(U_\chi)^2 \right] + \frac{6a_1}{\eta^8} \kappa^2 \left[\frac{6}{\chi}(U_\chi)^3 - \frac{3}{\chi^3}U^2 U_\chi + \frac{3}{\chi^2}U^2 U_{\chi\chi} \right. \\ & \left. + \frac{3}{\chi^2}U(U_\chi)^2 - \frac{6}{\chi^4}U^3 + \frac{1}{\chi^2}U(W_\chi)^2 - \frac{81}{3\chi}UW_\chi W_{\chi\chi} + \frac{8}{\chi}UU_\chi U_{\chi\chi} - \frac{101}{3\chi}U_\chi(W_\chi)^2 \right. \\ & \left. - \frac{20}{3}U_\chi W_\chi W_{\chi\chi} - \frac{10}{3}(W_\chi)^2 U_{\chi\chi} + 10(U_\chi)^2 U_{\chi\chi} \right] + A_6 = a_2 U_{\tau\tau} + c_{10} U_\tau \\ & 2a_1 \left(1 - \frac{1}{\eta^6} \right) \left(\frac{1}{\chi}W_\chi + W_{\chi\chi} \right) + \frac{6a_1}{\eta^7} \kappa \left(\frac{2}{\chi}U_\chi W_\chi + \frac{4}{3\chi}UW_{\chi\chi} + \frac{8}{3}W_\chi U_{\chi\chi} + \frac{8}{3}U_\chi W_{\chi\chi} \right) \\ & + \frac{6a_1}{\eta^8} \kappa^2 \left[\frac{1}{\chi^3}U^2 W_\chi - \frac{2}{\chi^2}UU_\chi W_\chi - \frac{1}{\chi^2}U^2 W_{\chi\chi} - \frac{6}{\chi}W_\chi(U_\chi)^2 - \frac{8}{3\chi}UW_\chi U_{\chi\chi} \right. \\ & \left. - \frac{20}{3}U_\chi W_\chi U_{\chi\chi} - \frac{10}{3}(U_\chi)^2 W_{\chi\chi} - \frac{8}{3\chi}UU_\chi W_{\chi\chi} + \frac{2}{3\chi}(W_\chi)^3 + 2(W_\chi)^2 W_{\chi\chi} \right] + A_7 = a_2 W_{\tau\tau} + c_{20} W_\tau - P \end{aligned} \right. \tag{35}$$

where a_1 and a_2 are

$$\begin{cases} a_1 = \frac{\sum_{i=1}^{N_L} \int_{h_i}^{h_{i+1}} C_{10(i)} dz}{h} \\ a_2 = \frac{\sum_{i=1}^{N_L} \int_{h_i}^{h_{i+1}} \gamma_{1(i)} dz}{h} \end{cases} \quad (36)$$

$$\chi_i = \frac{1}{2} \left[1 - \cos \left(\frac{i-1}{N-1} \pi \right) \right] \quad (i = 1, 2, 3, \dots, N) \quad (38)$$

Substituting Eq. (37) into Eq. (35), the governing equations are cast as

$$\begin{cases} a_{11} \left(\sum_{m=1}^N c_{im}^{(2)} U_m - \frac{1}{\chi_i} U_i + \frac{1}{\chi_i} \sum_{m=1}^N c_{im}^{(1)} U_m \right) \\ - a_{44} \left[\frac{1}{\chi_i^3} U_i^2 \sum_{m=1}^N c_{im}^{(1)} U_m - \frac{1}{\chi_i} U_i^2 \sum_{m=1}^N c_{im}^{(2)} U_m - \frac{1}{\chi_i} U_i \left(\sum_{m=1}^N c_{im}^{(1)} U_m \right)^2 + \frac{1}{\chi_i} U_i \left(\sum_{m=1}^N c_{im}^{(1)} W_m \right)^2 \right] \\ - a_{33} \left[\frac{1}{\chi_i^3} U_i^2 - \frac{2}{\chi_i} U_i \sum_{m=1}^N c_{im}^{(2)} U_m - \frac{1}{\chi_i} \left(\sum_{m=1}^N c_{im}^{(1)} U_m \right)^2 + \frac{1}{\chi_i} \left(\sum_{m=1}^N c_{im}^{(1)} W_m \right)^2 \right] + A_8 + A_9 = a_2 \ddot{U}_i + c_{10} \dot{U}_i \\ a_{22} \left(\sum_{m=1}^N c_{im}^{(2)} W_m + \frac{1}{\chi_i} \sum_{m=1}^N c_{im}^{(1)} W_m \right) + a_{33} \left[\frac{2}{\chi_i} \sum_{m=1}^N c_{im}^{(1)} U_m \sum_{m=1}^N c_{im}^{(1)} W_m + \frac{2}{\chi_i} U_i \sum_{m=1}^N c_{im}^{(2)} W_m \right] \\ + a_{44} \left[\frac{2}{\chi_i^2} U_i \sum_{m=1}^N c_{im}^{(1)} U_m \sum_{m=1}^N c_{im}^{(1)} W_m - \frac{U_i^2}{\chi_i^3} \sum_{m=1}^N c_{im}^{(1)} W_m + \frac{1}{\chi_i^2} U_i^2 \sum_{m=1}^N c_{im}^{(2)} W_m \right] + A_{10} + A_{11} = a_2 \ddot{W}_i + c_{20} \dot{W}_i - P \end{cases} \quad (39)$$

The terms A_6 and A_7 , which pertain to the dielectric properties of the composites, are given in Appendix 1.

The current study employs the DQ method to discretize the dimensionless governing equations, and the displacements and their derivatives of the membrane are defined as [50]

$$\begin{cases} \{U, W\} = \sum_{m=1}^N l_m(\chi) \{U_m, W_m\} \\ \left. \frac{\partial^k \{U, W\}}{\partial \chi^k} \right|_{\chi=\chi_i} = \sum_{m=1}^N c_{im}^{(k)} \{U_m, W_m\} \end{cases} \quad (37)$$

where N represents the sum of discrete points along the membrane’s radius, U_m and W_m represent the radial and transversal displacements at $\chi = \chi_m$, respectively. The Lagrange interpolation function is represented by $l_m(\chi)$, and the weighting coefficient of the k th derivative is represented by $c_{im}^{(k)}$. Then the distribution of grid points is as follows

The coefficients related to the applied voltage in Eq. (39) become

$$\begin{cases} a_{11} = 2a_1 \left(1 + \frac{3}{\eta^6} \right) + b_1 \eta^2 \\ a_{22} = 2a_1 \left(1 - \frac{1}{\eta^6} \right) + b_1 \eta^2 \\ a_{33} = b_1 \kappa \eta \\ a_{44} = b_1 \kappa^2 \end{cases} \quad (40)$$

A_8, A_9, A_{10} and A_{11} in Eq. (39) related to the radial and transversal motions are given in Appendix 1.

Correspondingly, the associated boundary conditions become

$$\begin{cases} U(0, \tau) = U(1, \tau) = 0 \\ W(1, \tau) = 0 \end{cases} \quad (41)$$

Equation (39) can also be written in a matrix form as

$$M\ddot{d} + C\dot{d} + (K_L + K_{NL})d = P \tag{42}$$

where M and C represent matrices for mass and energy damping coefficient, respectively, K_L and K_{NL} represent linear and nonlinear stiffness matrix, respectively, depending on displacement vector $d = \{\{U_i\}^T, \{W_i\}^T\}^T (i = 1, 2, 3, \dots, N)$, and P is the base excitation vector. The linear stiffness matrix K_L is expressed as

$$K_L = \begin{pmatrix} -\frac{1}{\chi^2}a_{11}I + \frac{1}{\chi}a_{11}c^{(1)} + a_{11}c^{(2)} & \mathbf{0} \\ \mathbf{0} & \frac{1}{\chi}a_{22}c^{(1)} + a_{22}c^{(2)} \end{pmatrix} \tag{43}$$

The detail of the nonlinear stiffness matrix K_{NL} is given in Appendix 2.

In present work, incremental harmonic balance (IHB) method is employed to solve the equations mentioned above. The equations involve a base excitation term, defined as $P = P_0 \cos(\Omega\tau)$, where P_0 represents a generalized force vector. $T = \Omega\tau$ is introduced, which allows Eq. (42) to be cast as

$$\Omega^2 M\ddot{d} + \Omega C\dot{d} + (K_L + K_{NL})d = P_0 \cos(T) \tag{44}$$

Assuming that $d_{0\Gamma}$ and Ω_0 represent the displacement and frequency of a state of vibration, its adjacent state can be represented by adding an increment, i.e.

$$d_\Gamma = d_{0\Gamma} + \Delta d_\Gamma, \quad \Omega = \Omega_0 + \Delta\Omega \quad \Gamma = 1, 2, \dots, 2N \tag{45}$$

Upon substituting Eq. (45) into Eq. (44) and neglecting higher order infinitesimal terms, we obtain

$$\Omega_0^2 M\Delta\ddot{d} + \Omega_0 C\Delta\dot{d} + (K_L + \tilde{K}_{NL})\Delta d = R - (2\Omega_0 M\ddot{d}_0 + C\dot{d}_0)\Delta\Omega \tag{46}$$

where

$$R = P_0 \cos(T) - [\Omega_0^2 M\ddot{d}_0 + \Omega_0 C\dot{d}_0 + (K_L + K_{NL})d_0] \tag{47}$$

$$\tilde{K}_{NL} = \begin{bmatrix} 2K_{NL}^{11}(1) + 3K_{NL}^{11}(2) & 2K_{NL}^{12}(1) + 3K_{NL}^{12}(2) \\ 2K_{NL}^{21}(1) + 3K_{NL}^{21}(2) & 2K_{NL}^{22}(1) + 3K_{NL}^{22}(2) \end{bmatrix} \tag{48}$$

$$d_0 = [d_{01}, d_{02}, \dots, d_{0(2N-1)}, d_{0(2N)}]^T \tag{49}$$

and

$$\Delta d = [\Delta d_1, \Delta d_2, \dots, \Delta d_{2N-1}, \Delta d_{2N}]^T \tag{50}$$

Both the solution $d_{0\Gamma}$ and increment Δd_Γ can be expressed via the Fourier series expansion

$$\begin{cases} d_{0\Gamma} = a_{0\Gamma 0} + \sum_{i=1}^{N_c} a_{0\Gamma i} \cos(iT) + \sum_{i=1}^{N_s} b_{0\Gamma i} \sin(iT) = X_s Z_{0\Gamma} \\ \Delta d_\Gamma = \Delta a_{\Gamma 0} + \sum_{i=1}^{N_c} \Delta a_{\Gamma i} \cos(iT) + \sum_{i=1}^{N_s} \Delta b_{\Gamma i} \sin(iT) = X_s \Delta Z_\Gamma \end{cases} \quad \Gamma = 1, 2, \dots, 2N \tag{51}$$

where

$$\begin{cases} X_s = [1, \cos(T), \cos(2T), \dots, \cos(N_c T), \sin(T), \sin(2T), \dots, \sin(N_s T)] \\ Z_{0\Gamma} = [a_{0\Gamma 0}, a_{0\Gamma 1}, a_{0\Gamma 2}, \dots, a_{0\Gamma N_c}, b_{0\Gamma 1}, b_{0\Gamma 2}, \dots, b_{0\Gamma N_s}]^T \\ \Delta Z_\Gamma = [\Delta a_{\Gamma 0}, \Delta a_{\Gamma 1}, \Delta a_{\Gamma 2}, \dots, \Delta a_{\Gamma N_c}, \Delta b_{\Gamma 1}, \Delta b_{\Gamma 2}, \dots, \Delta b_{\Gamma N_s}]^T \end{cases} \tag{52}$$

Assuming that the numbers of sine and cosine terms of the Fourier series in Eq. (52) are equal, i.e., $N_c = N_s = a$, then substituting Eq. (51) into Eqs. (49) and (50) results in

$$d_0 = S Z_0, \quad \Delta d = S \Delta Z \tag{53}$$

where

$$\begin{cases} S = \text{diag}[X_s, X_s, \dots, X_s]_{2N} \\ Z_0 = [Z_{01}, Z_{02}, \dots, Z_{0(2N)}]^T \\ \Delta Z = [\Delta Z_1, \Delta Z_2, \dots, \Delta Z_{2N}]^T \end{cases} \tag{54}$$

By substituting Eq. (53) into Eq. (46) and using the Galerkin procedure, we can derive a linear equation in terms of the increments ΔZ and $\Delta\Omega$, given by

$$K_{mc} \Delta Z = \bar{R} - R_{mc} \Delta\Omega \tag{55}$$

where

$$\begin{cases} K = \int_0^{2\pi} [S^T \Omega_0^2 M \mathcal{F} + \Omega_0 C S + (K_L + \tilde{K}_{NL}) S] dT \\ \bar{R} = \int_0^{2\pi} S^T \{P_0 \cos(T) - [\Omega_0^2 M \mathcal{F} + \Omega_0 C S + (K_L + K_{NL}) S] Z_0\} dT \\ R = \int_0^{2\pi} S^T (2\Omega_0 M \mathcal{F} + C S) Z_0 dT \end{cases} \tag{56}$$

To begin the solution process, a guessed value of Ω_0 can be used to obtain both linear and nonlinear solutions. The dynamic responses of the structure can be calculated point by point by increasing the frequency Ω or a component of the coefficient vector Z_0 . Furthermore, the nonlinear multi-valued solution is

obtained using an incremental arc-length continuation technique to improve computational efficiency [51].

5 Results and discussions

In current work, the following parameters will be adopted in the calculation unless specifically indicated [10, 17, 52]

- The dimensions of the membrane are $b = 0.008$ m and $h = 0.0002$ m, respectively, and the radial stretching ratio is $\eta = 1.01$;
- The amplitude of excitation is $P_0 = 0.1$ and the damping ratio is $\zeta = 0.1$;
- The diameter and thickness of the GNP filler are $D_{\text{GNP}} = 8.1967 \times 10^{-6}$ m and $t_{\text{GNP}} = 5 \times 10^{-8}$ m, respectively;
- The average volume fraction of GNPs is $\varphi_{\text{avg}} = 1.6\%$ and the slope factor is $S_g = 0.2$;
- For the matrix PVDF, the density is $\gamma_m = 1780$ kg/m³. The elastic modulus and Poisson’s ratio are $E_m = 1.44$ GPa and $\nu_m = 0.35$. The electrical conductivity is $\sigma_m = 3.5 \times 10^{-9}$ S/m and the dielectric permittivity is $\epsilon_m = 5 \times 8.85 \times 10^{-12}$ F/m;
- For the filler GNP, the density is $\gamma_{\text{GNP}} = 2200$ kg/m³. The elastic modulus and Poisson’s ratio are $E_1 = E_2 = 1.01$ TPa, $E_3 = 101$ TPa and $\nu_{\text{GNP}} = 0.175$. The in-plane and out-of-plane electrical conductivity are $\sigma_1 = \sigma_2 = 8.32 \times 10^4$ S/m and

$\sigma_3 = 83.2$ S/m, respectively. The in-plane and out-of-plane dielectric permittivity are $\epsilon_1 = \epsilon_2 = 1.3275 \times 10^{-10}$ F/m and $\epsilon_3 = 8.89425 \times 10^{-11}$ F/m, respectively;

- For the internal pore, the density is $\gamma_p = 1.293$ kg/m³. The electrical conductivity is $\sigma_p = 1 \times 10^{-15}$ S/m and the dielectric permittivity is $\epsilon_p = 8.85 \times 10^{-12}$ F/m. The pore aspect ratio is $\alpha_p = 0.01$ and porosity is $n = 0.1$.

5.1 Convergence and validation study

To achieve accurate results in the discretization process employing the DQ method, a larger number of grid points is typically required. However, an increase in grid points can also result in a greater demand for computational resources. Balancing accuracy and computational efficiency, a convergence analysis is conducted to determine the minimum number of grid points needed. Table 1 tabulates the dimensionless amplitudes of the membrane for different electrical and base excitations considering different orders of Fourier series a . As observed, the effect of the order of the Fourier series is negligible, which may be attributed to the reason that the excitation frequency is selected around the frequency of the first harmonic terms, and the results converge when $N = 17$. Therefore, $N = 17$ will be used for subsequent calculation unless otherwise specified.

Table 1 Convergence study on the number of grid points

a	N	$V_{\text{DC}} = 0$ V		$V_{\text{DC}} = 10$ V		$V_{\text{DC}} = 20$ V	
		$P_0 = 0.1$	$P_0 = 0.5$	$P_0 = 0.1$	$P_0 = 0.5$	$P_0 = 0.1$	$P_0 = 0.5$
1	7	0.45400	2.22700	0.47115	2.35574	0.57291	2.86457
	9	0.43886	2.19430	0.45234	2.26172	0.54412	2.72061
	11	0.42296	2.11484	0.44262	2.21312	0.51709	2.58544
	13	0.41371	2.06853	0.43971	2.19856	0.48418	2.42106
	15	0.41240	2.06203	0.43625	2.18124	0.47596	2.37982
	17	0.41240	2.06203	0.43625	2.18124	0.47596	2.37982
	19	0.41240	2.06203	0.43625	2.18124	0.47596	2.37982
2	7	0.45400	2.22700	0.47115	2.35574	0.57291	2.86457
	9	0.43886	2.19430	0.45234	2.26172	0.54412	2.72061
	11	0.42296	2.11484	0.44262	2.21312	0.51709	2.58544
	13	0.41371	2.06853	0.43971	2.19856	0.48418	2.42106
	15	0.41240	2.06203	0.43625	2.18124	0.47596	2.37982
	17	0.41240	2.06203	0.43625	2.18124	0.47596	2.37982
	19	0.41240	2.06203	0.43625	2.18124	0.47596	2.37982

Table 2 Dependency of the dimensionless amplitude on the number of gradient layers

n	Z	X		O		A		V	
		0	20	0	20	0	20	0	20
0.1	6	0.38467	0.42017	0.42861	0.46002	0.41702	0.45215	0.40579	0.44776
	8	0.38626	0.42405	0.42721	0.45925	0.41683	0.45308	0.40607	0.44879
	10	0.38749	0.42723	0.42597	0.45848	0.41669	0.45362	0.40626	0.44939
	20	0.38802	0.42931	0.42471	0.45813	0.41661	0.45411	0.40635	0.44952
	40	0.38809	0.42939	0.42457	0.45798	0.41658	0.45419	0.40641	0.44959
	80	0.38815	0.42946	0.42448	0.45789	0.41655	0.45428	0.40645	0.44963
0.5	6	1.35401	1.69498	1.50145	1.84368	1.46571	1.81312	1.42624	1.79652
	8	1.35669	1.69726	1.49753	1.84059	1.46504	1.81685	1.42723	1.79965
	10	1.35792	1.69918	1.49517	1.83851	1.46455	1.81902	1.42789	1.80205
	20	1.35969	1.70163	1.49374	1.83712	1.46427	1.82098	1.42821	1.80258
	40	1.35982	1.70175	1.49356	1.83701	1.46417	1.82109	1.42827	1.80266
	80	1.35991	1.70183	1.49349	1.83693	1.46409	1.82122	1.42832	1.80272

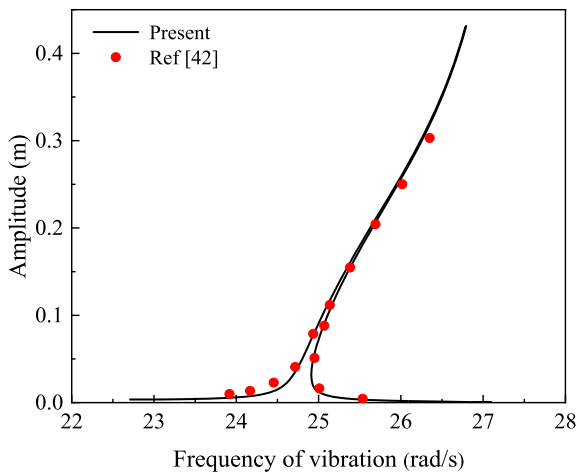


Fig. 6 Comparison between present results and Ref [42]

In addition to the convergence analysis of the grid points, Table 2 presents the number of layers required to obtain the FG-GNPRC dielectric porous membrane. It can be seen that the dimensionless amplitude gradually converges as the number of layers increases. Balancing the accuracy and efficiency of the calculation, 20 layers will be used for the structural analysis.

To validate the proposed model and the solution, Fig. 6 verifies the amplitude-frequency curves with the previously reported results [42] without considering dielectric properties. The material properties and structural dimensions are chosen as $b = 1$ m, $h = 0.001$ m, $\gamma = 2200$ kg·m⁻³ and $C_1 = 0.17$ MPa,

respectively. The results obtained by present work agree well with the ones in existing studies.

Further validation is conducted by finite element analysis (FEA) considering the internal pores. Abaqus is adopted for FEA and a total number of 8164 C3D10 elements are used for the membrane. Comparison of FEA results with the one by the present model for the nonlinear frequency response is depicted in Fig. 7. Excellent agreement is observed between the FEA and our numerical results. It is found that the membrane with relatively large porosity exhibits larger amplitude and stronger nonlinear hardening behavior.

5.2 Parametric study

Figure 8 exhibits the variation of the dimensionless amplitude of the FG-GNPRC membrane with the slope factor S_g . It can be found that the increase of S_g engenders a gradual decrease in the susceptibility of the composite membrane’s amplitude to the influence of the applied voltage. Furthermore, the amplitude ceases to be influenced by voltage when S_g exceeds a certain value. The above observation can be attributed to the dependency of the dielectric properties of the FG-GNPRC membrane on S_g . When S_g exceeds a certain value, the presence of a percolation threshold leads to the lowest GNP concentration layer’s dielectric properties to be negligible, and thus the applied electric field becomes incapable of altering the structural behavior of the FG-GNPRC membrane.

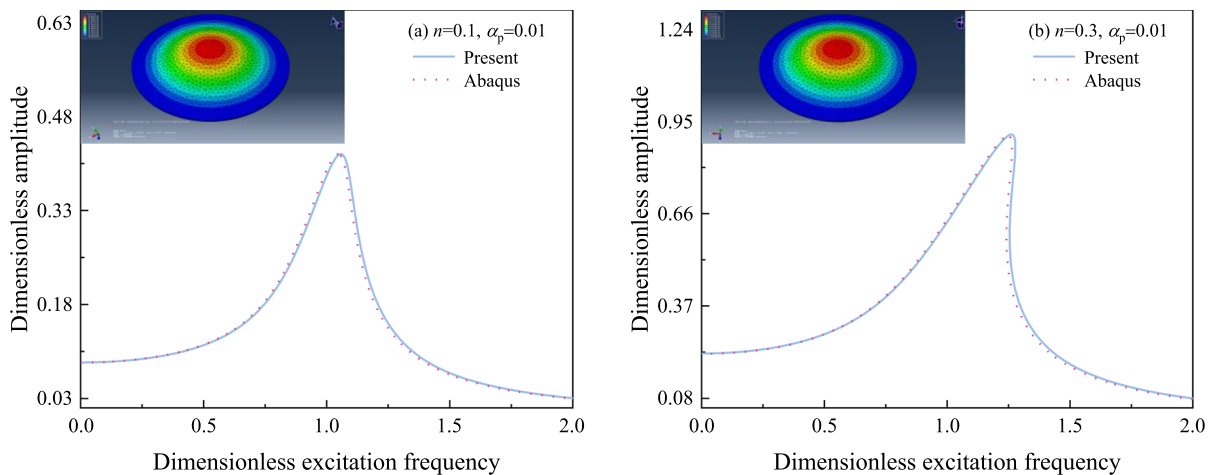


Fig. 7 Comparison of FEA results with the present model for the nonlinear frequency response of FG-GNPRC membrane **a** $n = 0.1$, **b** $n = 0.3$

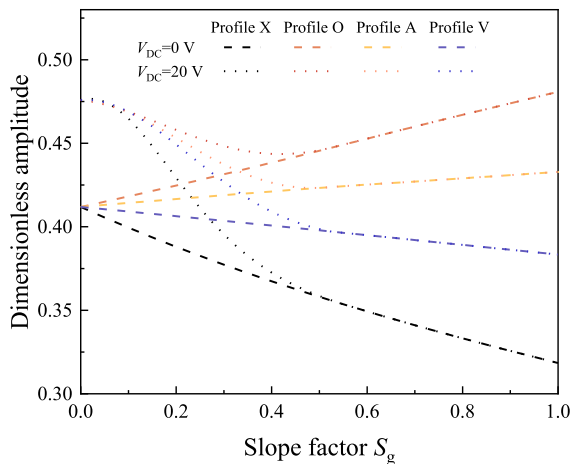


Fig. 8 Dependency of the dimensionless amplitude on slope factor S_g

Such a phenomenon highlights the influence of S_g on the dimensionless amplitude of the FG-GNPRC membrane subjected to electro-mechanical loading, indicating the vital role of percolation in governing the dielectric behavior of the FG-GNPRC membrane.

Figure 9 presents the effect of thickness-to-radius ratio on the dimensionless amplitude of FG-GNPRC membrane. As observed, with the application of the electrical field, the dimensionless amplitudes of FG-GNPRC membranes with different profiles exhibit a decline as κ increases, indicating a nonlinear effect of κ on the system. For example, in Fig. 9a, when the applied voltage is 20 V, for a membrane with a fixed radius of 8 mm, when κ increases from 0.02 to 0.03,

the dimensionless amplitude decreases by 26.8%, while the decrease is only 7.2% as κ further increases from 0.03 to 0.04.

Figure 10 investigates the dependency of the dimensionless amplitude on AC frequency and DC voltage. Upon observation, as the applied voltage increases, two transition regions are emerged where the amplitude is highly sensitive to the AC frequency. For the first transition, i.e., $f_{AC} = 10^{-3}$ Hz, the dielectric permittivity of the FG-GNPRC membrane increases abruptly. This is because the GNP is separated by an extremely thin dielectric layer of PVDF, which accumulates a large number of interfacial charges. As a result, many charges are trapped at the filler-polymer interface due to the effect of Maxwell-Wagner-Sillars (MWS) polarization. For the second transition, i.e., $f_{AC} = 10^2$ Hz, the number of accumulated electrons decreases due to additional electron tunneling within the GNP interface layer at higher AC frequency. This leads to a decrease in the effect of MWS polarization. Furthermore, a comparison between Fig. 10a and b evidences that as S_g increases, the effect of MWS polarization decreases significantly. This can be elucidated by a reduction in charge accumulation within the FG-GNPRC membrane, leading to a decrease in dielectric properties.

Figure 11 discusses the dependency of the dimensionless amplitude on the aspect ratio of pore α_p and porosity n . In Fig. 11a, it can be found that the dimensionless amplitude increases with increasing n , and the trend is more pronounced for the FG-GNPRC

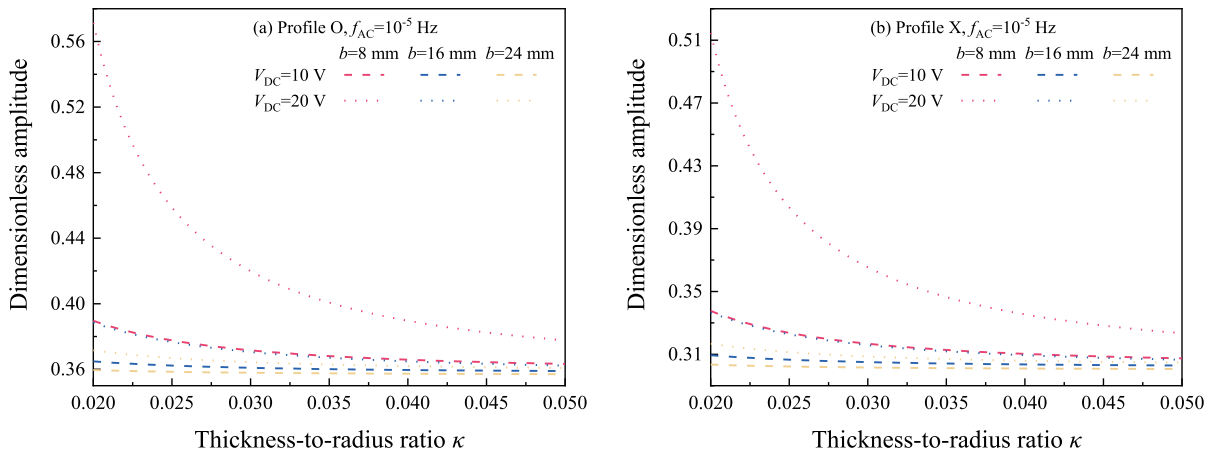


Fig. 9 Dependency of the dimensionless amplitude on thickness-to-radius ratio κ for **a** profile O and **b** profile X

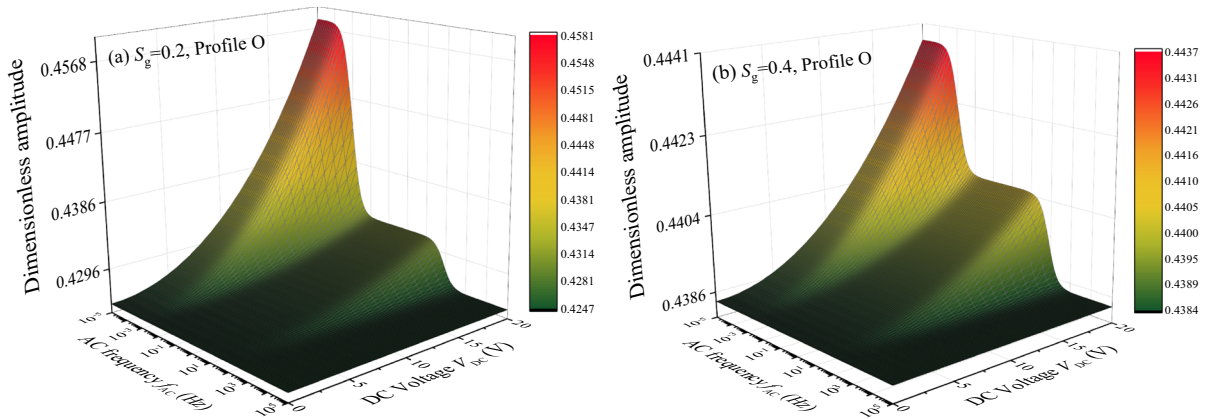


Fig. 10 Dependency of dimensionless amplitude on AC frequency f_{AC} and DC voltage V_{DC} **a** $S_g = 0.2$, **b** $S_g = 0.4$

membrane with relatively small α_p of internal pore. Moreover, the observation becomes more evident after the application of the external electric field. Compared with Fig. 11a, the effect of the external electric field in Fig. 11b is relatively small. These phenomena can be explained by the dependency of the stiffness of the FG-GNPRC membrane on the attribute of pore and the stretching ratio. Pores with relatively small α_p are prone to developing into microcrack patterns, which can significantly affect the mechanical robustness of the FG-GNPRC membrane due to the difference in mechanical properties and surface properties. For the FG-GNPRC membrane subjected to larger stretch, the increased stiffness of the system affects the regulation of the structural behavior by the applied voltage. Such an observation suggests that the effect of the applied

voltage on structural behavior can be managed by adjusting the stretching ratio.

Figure 12 shows the dependency of the dimensionless amplitude on pore aspect ratio α_p and GNP diameter-to-thickness ratio D_{GNP}/t_{GNP} . The applied voltage is fixed as 20 V. In Fig. 12a, the dimensionless amplitude is relatively large for smaller or larger D_{GNP}/t_{GNP} with changing pore aspect ratio, which can be explained by the competing effects of mechanical and electrical properties on structural behavior of the FG-GNPRC membrane. When D_{GNP}/t_{GNP} is smaller, the mechanical properties dominate and the structural behavior is mainly related to the variation of the elastic modulus. However, as D_{GNP}/t_{GNP} increases, the dielectric properties of the FG-GNPRC membrane exert a substantial influence on the structural behavior,

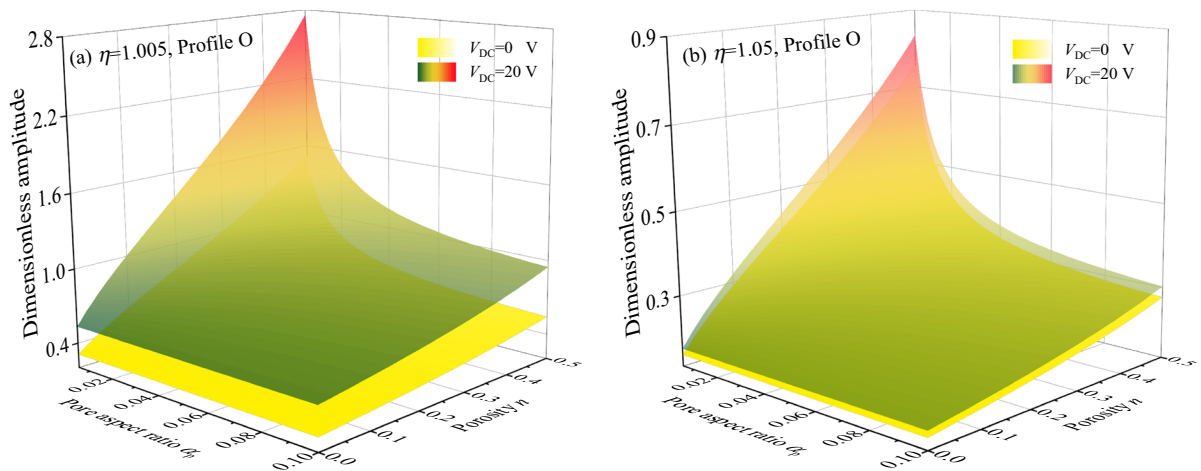


Fig. 11 Dependency of dimensionless amplitude on pore aspect ratio α_p and porosity n **a** $\eta = 1.005$, **b** $\eta = 1.05$

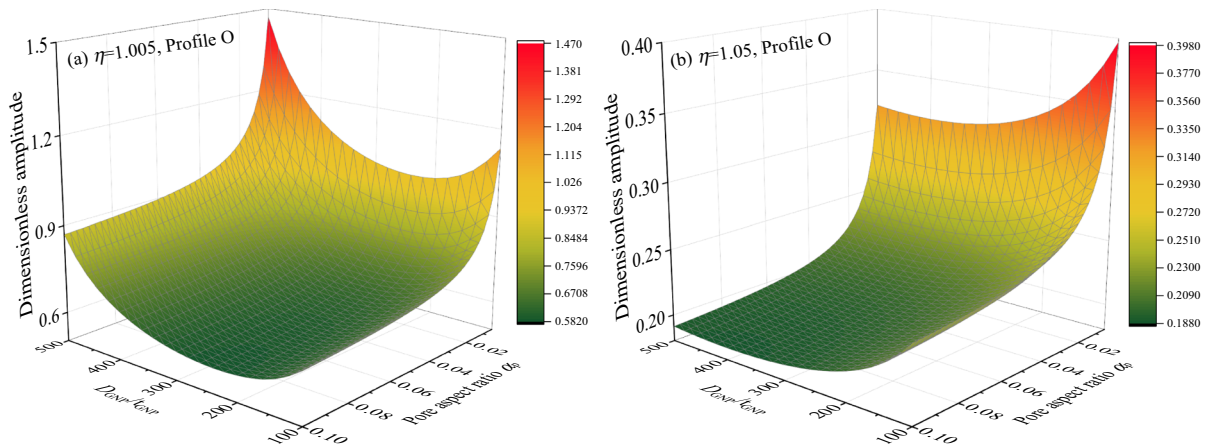


Fig. 12 Dependency of dimensionless amplitude on pore aspect ratio α_p and GNP diameter-to-thickness ratio $D_{\text{GNP}}/t_{\text{GNP}}$ **a** $\eta = 1.005$, **b** $\eta = 1.05$

resulting in an increase in the structural amplitude. In contrast, Fig. 12b reveals a distinct phenomenon where the dimensionless amplitude of the FG-GNPRC membrane is notably reduced at $D_{\text{GNP}}/t_{\text{GNP}} = 500$ in comparison to $D_{\text{GNP}}/t_{\text{GNP}} = 100$. This once again underscores the ability to actively manipulate the effect of the applied voltage on structural behavior by altering the stretching ratio of the FG-GNPRC membrane.

Figure 13 presents the variation of the frequency response of the FG-GNPRC membrane for different

stretching ratios. It can be seen that the excitation frequency of the system generating the peak amplitude increases as the stretching ratio increases, while the maximum dimensionless amplitude decreases with increasing stretching ratio. Moreover, the system displays a stronger hardening behavior and wider multi-valued response region for relatively small stretching ratio. The above observation can be attributed to the fact that the natural frequency of the system increases as the stretching ratio increases. In addition, it can be observed that there exists a certain

excitation frequency generating the identical amplitude for the FG-GNPRC membrane with different stretching ratios, and the identical amplitude between the membranes is larger for those with larger stretching ratios. This reflects that there exists an energy transfer mechanism between different stretched membranes.

Figure 14 shows the frequency response of the FG-GNPRC membrane subjected to different damping ratios. Expectedly, the dimensionless amplitude decreases with the increase of the damping ratio, while the influence becomes limited when the damping ratio increases to a relatively large value. In

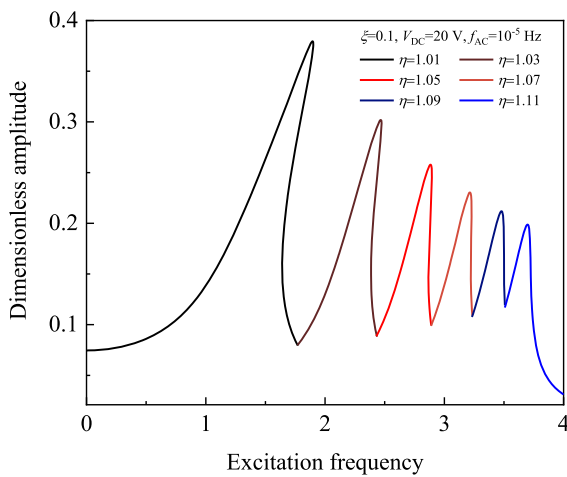
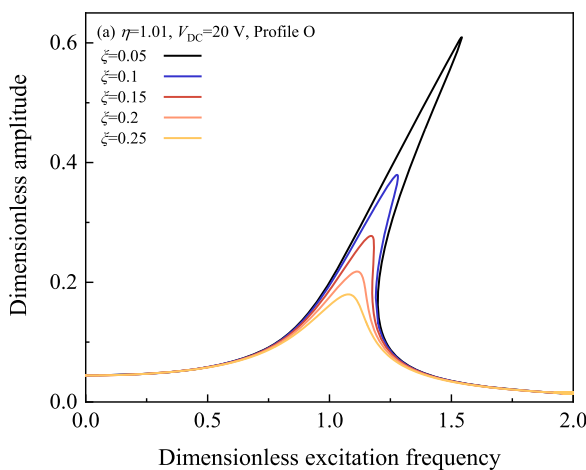


Fig. 13 Nonlinear frequency response of the FG-GNPRC membrane with different stretching ratios in profile O



addition, similar to the above observation, with the increase of the stretching ratio, the nonlinearity of the system becomes weaker and the multi-valued response region decreases.

Figure 15 investigates the influence of different membrane thickness h and thickness-to-radius ratio κ on the frequency response of the FG-GNPRC membrane. In Fig. 15a, when there is no electrical loading, the frequency response remains consistent for different h at the same κ . However, when the external electric field is applied, the effect of DC voltage is noticeable for relatively small h , i.e., $h = 0.1 \text{ mm}$, resulting in a stronger nonlinear response of the membrane. The above observation can be attributed to the high dependency of the Helmholtz free energy on the membrane thickness as indicated in Eqs. (19), (23) and (27). This phenomenon is more pronounced for altering only the thickness while keeping the radius b constant, as shown in Fig. 15b. When the radius of the membrane is fixed as 8 mm, and κ decreases only from 0.025 to 0.02, the frequency response becomes highly nonlinear and the structural hardening behavior is obvious.

Figure 16 displays the effect of different GNP weight fraction f_{GNP} and GNP diameter-to-thickness ratio D_{GNP}/t_{GNP} on the frequency response. As seen in Fig. 16a, for relatively small f_{GNP} , i.e., $f_{GNP} = 0.5\%$, the frequency response is barely influenced by the electrical loading. While f_{GNP} is relatively large, i.e., $f_{GNP} = 2.0\%$, the effect of the external electric field on the frequency response of the system becomes

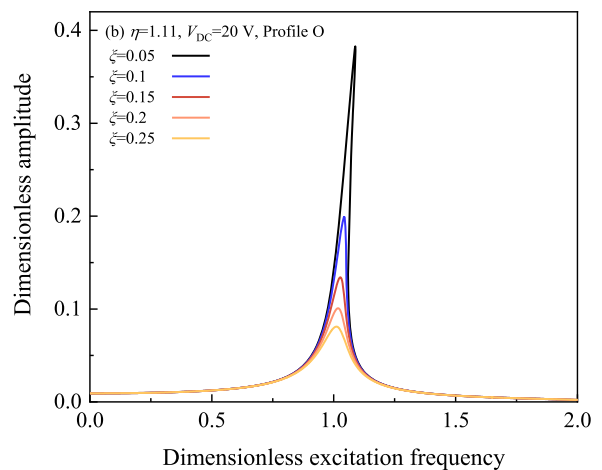


Fig. 14 Nonlinear frequency response of the FG-GNPRC membrane with different damping ratios **a** $\eta = 1.01$ **b** $\eta = 1.11$

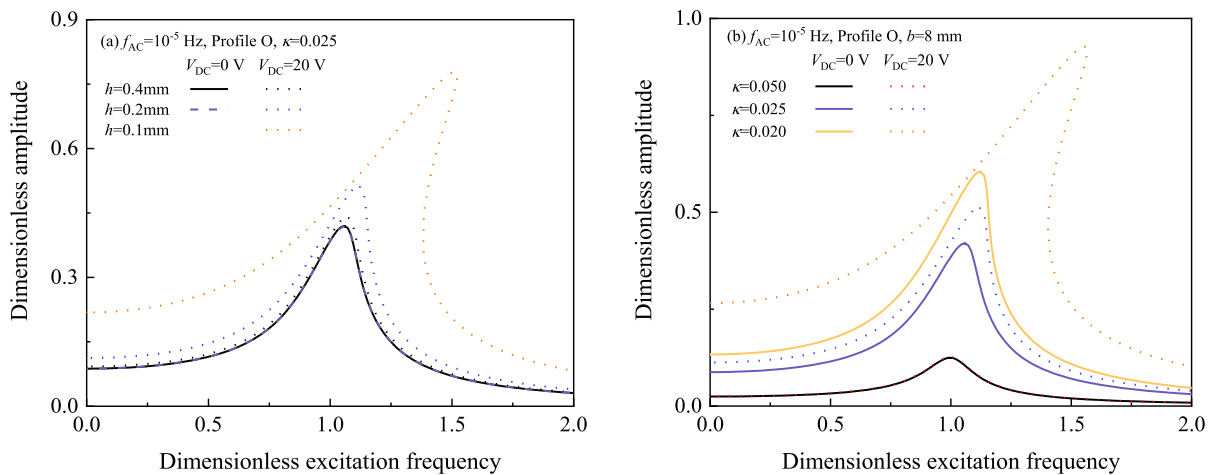


Fig. 15 Nonlinear frequency response of the FG-GNPRC membrane with different DC voltages and **a** membrane thickness h **b** thickness-to-radius ratio κ

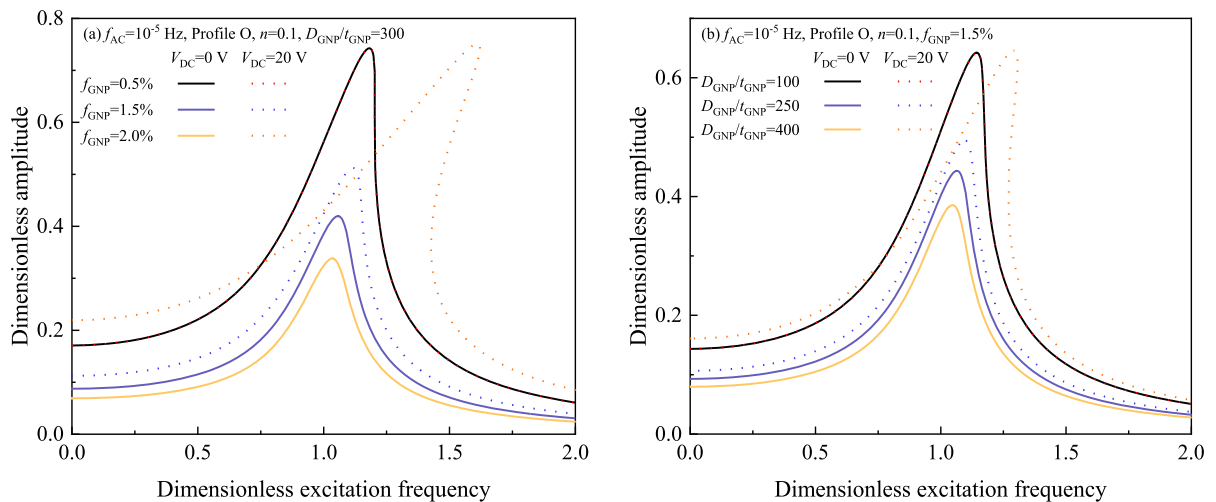


Fig. 16 Nonlinear frequency response of the FG-GNPRC membrane with different DC voltages and **a** GNP weight fraction f_{GNP} **b** GNP diameter-to-thickness ratio $D_{\text{GNP}}/t_{\text{GNP}}$

apparent. The FG-GNPRC membrane under the applied electric field shows a noticeable nonlinear frequency response and exhibits a stronger hardening behavior compared with the one without electrical loading. Similar observations can be found in Fig. 16b. For relatively small $D_{\text{GNP}}/t_{\text{GNP}}$, i.e., $D_{\text{GNP}}/$

$t_{\text{GNP}} = 100$, there exists limited hardening behavior of the FG-GNPRC membrane. However, when $D_{\text{GNP}}/t_{\text{GNP}}$ is relatively large, i.e., $D_{\text{GNP}}/t_{\text{GNP}} = 400$, the dynamic response of FG-GNPRC is significantly altered under the action of the external electric field. This can also be attributed to the dependency of the

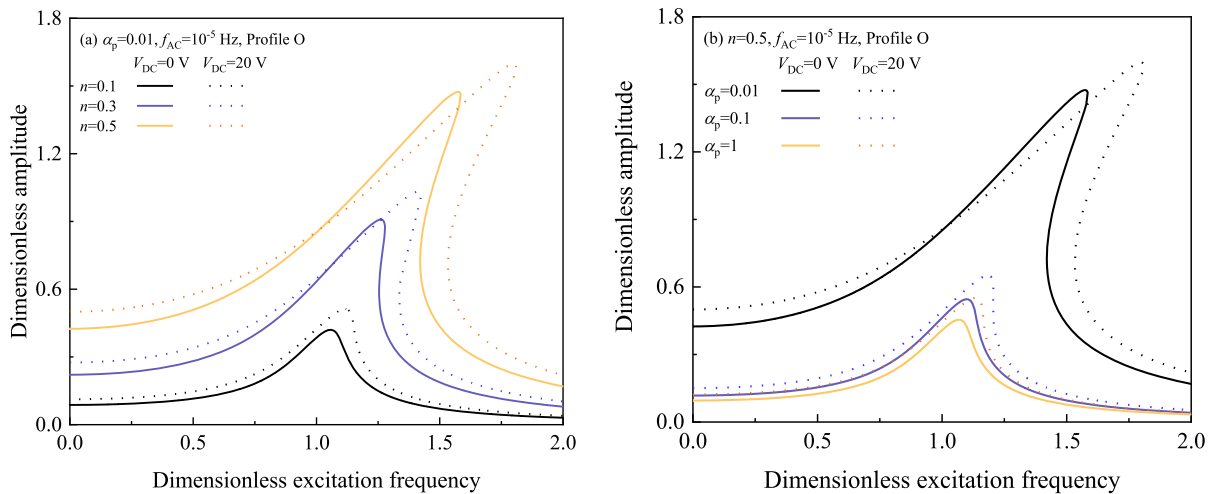


Fig. 17 Nonlinear frequency response of the FG-GNPRC membrane with different DC voltages and **a** porosity n **b** pore aspect ratio α_p

dielectric permittivity of the FG-GNPRC membrane on the percolation threshold. Below the percolation threshold, the dynamic response of the system influenced by the applied voltage is very limited, and when GNP concentration exceeds the percolation threshold, the resonance behavior of the FG-GNPRC membrane can be adjusted by varying the applied voltage.

Figure 17 investigates the influence of different porosity n and pore aspect ratio α_p on the frequency response of the FG-GNPRC membrane. In Fig. 17a, for the same α_p , it can be clearly seen that the amplitude increases with increasing n and the applied voltage increases both the amplitude and hardening behavior, particularly for membranes with relatively large n . In Fig. 17b, it is found that pore aspect ratio α_p has a significant effect on the frequency response, for relatively small α_p , i.e., $\alpha_p = 0.01$, the system displays a stronger hardening behavior and a higher peak amplitude frequency. In addition, it is seen that the maximum dimensionless amplitude of the oscillations increases as a result of decreased α_p . The above observation can be attributed to the effect of internal pore on the electrical and mechanical properties of the composite membrane. Such narrow and long pores have an obstructive effect and these pores are

developed into micro-crack patterns in certain directions. Their insulating property can disrupt the formed conductive networks and block the transmission channels of the carrier. Moreover, the formation of these microcracks also reduce the stiffness of the composite membrane.

6 Conclusion

The nonlinear dynamics of the FG-GNPRC membrane subjected to electro-mechanical loading is analyzed numerically taking into account the effects of internal pores, dimension of the membrane and other factors. The strain energy of the system is obtained by means of the hyperelastic membrane theory, Neo-Hookean constitutive model and the couple dielectric theory. The energy expressions are inserted in the Hamilton's principle yielding a set of strongly nonlinear governing equations. The equations are discretized by combining TSE and DQ methods. IHB and arc-length continuation technique are then employed to perform a nonlinear analysis for comprehensive system parameters.

The analysis reveals that FG-GNPRC membrane with profile X exhibits the smallest dimensionless

amplitude, while the largest dimensionless amplitude can be obtained for the beam with profile O. The increase of S_g reduces the effect of the applied electrical load on the structural behavior of the FG-GNPRC membrane, as does the effect of MWS polarization. Therefore, S_g needs to be controlled within 0.5 to ensure that the amplitude of the membrane can be adjusted by varying the electric field. The presence of pores affects the structural behavior and stability of the system, especially for smaller pore aspect ratio. Additionally, the effect of the applied voltage on the structural behavior can be controlled by varying the stretching ratio. The FG-GNPRC membrane with a smaller stretching ratio exhibits stronger nonlinear hardening behavior, and the energy transfer mechanism is observed by varying the stretching ratio. When h and κ are relatively small, the applied voltage has a notable influence on the system, resulting in a more pronounced nonlinear hardening behavior. Moreover, it is demonstrated that the existence of internal pores has obvious influence on the nonlinear dynamic response of the membrane. The FG-GNPRC membrane with relatively small pore aspect ratio is more affected by the external electric load, generating a higher amplitude peak and excitation frequency required for the resonance.

Acknowledgements The authors greatly acknowledge the financial support from Innovative and Entrepreneurial Talents of Jiangsu Province of China and the Australian Research Council grant under the Discovery Project Scheme (DP210103656, DP230100548).

Author contributions ZN: Writing—original draft, Formal analysis, Methodology, Data curation. YF: Validation. JY: Visualization. ZH: Investigation. CF: Writing—review & editing, Conceptualization, Supervision, Funding acquisition. JY: Writing—review & editing, Funding acquisition.

Funding Innovative and Entrepreneurial Talents of Jiangsu Province of China, Australian Research Council, DP210103656, Jie Yang, DP230100548, Jie Yang.

Data availability The data that support the findings of this study are available from the corresponding authors upon reasonable request.

Declarations

Conflict of interest The authors declare that they have no known competing financial interests or personal relationships that could have appeared to influence the work reported in this paper.

Appendix 1

$$\begin{aligned}
 A_1 &= (\eta\rho + u)^3 \left[(\eta + u\rho)^2 + (w\rho)^2 \right]^3 \\
 A_2 &= \rho^2 \left[(\eta + u\rho)^2 + (w\rho)^2 \right]^2 - (\eta\rho + u) \left[(\eta + u\rho)^2 + (w\rho)^2 \right] \\
 &\quad \left[3\rho(\eta + u\rho) + \rho^2 u\rho\rho \right] \\
 &\quad + 2\rho^2 (\eta + u\rho)^2 \left[(\eta + u\rho)^2 + (w\rho)^2 \right] + 4\rho^2 (\eta + u\rho)(\eta\rho + u) \\
 &\quad \left[(\eta + u\rho)u\rho\rho + w\rho w\rho\rho \right] \\
 A_3 &= \left[(\eta + u\rho)^2 + (w\rho)^2 \right] \left[2\rho^2 w\rho(\eta + u\rho) \right. \\
 &\quad \left. - (3\rho w\rho + \rho^2 w\rho\rho)(\eta\rho + u) \right] + 4\rho^2 w\rho(\eta\rho + u) \\
 &\quad \left[(\eta + u\rho)u\rho\rho + w\rho w\rho\rho \right] \\
 A_4 &= -4\eta\lambda_1 u\rho u\rho\rho - \frac{10\lambda_1}{3} (w\rho)^2 u\rho\rho - \frac{20\lambda_1}{3} u\rho w\rho w\rho\rho \\
 &\quad + \frac{4\eta\lambda_1}{3} w\rho w\rho\rho + 10\lambda_1 (u\rho)^2 u\rho\rho \\
 A_5 &= -\frac{8\eta\lambda_1}{3} w\rho u\rho\rho + \frac{8\eta\lambda_1}{3} u\rho w\rho\rho - \frac{20\lambda_1}{3} u\rho w\rho u\rho\rho \\
 &\quad - \frac{10\lambda_1}{3} (u\rho)^2 w\rho\rho + 2\lambda_1 (w\rho)^2 w\rho\rho \\
 A_6 &= b_1 \eta^2 \left(-\frac{1}{\chi^2} U + \frac{1}{\chi} U_\chi + U_{\chi\chi} \right) - b_1 \kappa \left[\frac{\eta}{\chi^3} U^2 - \frac{2\eta}{\chi} U U_{\chi\chi} - \frac{\eta}{\chi} (U_\chi)^2 \right. \\
 &\quad \left. \kappa \frac{1}{\chi^3} U^2 U_\chi - \kappa \frac{U^2}{\chi^2} U_{\chi\chi} - \kappa \frac{1}{\chi^2} U (U_\chi)^2 + \frac{\eta}{\chi} (W_\chi)^2 + \kappa \frac{1}{\chi^2} U (W_\chi)^2 \right] \\
 A_7 &= b_1 \eta^2 \left(\frac{1}{\chi} W_\chi + W_{\chi\chi} \right) + b_1 \kappa \left[\frac{2\eta}{\chi} U_\chi W_\chi + \frac{2\eta}{\chi} U W_{\chi\chi} + \frac{2}{\chi^2} \kappa U U_\chi W_\chi \right. \\
 &\quad \left. - \frac{U^2}{\chi^3} \kappa W_\chi + \frac{U^2}{\chi^2} \kappa W_{\chi\chi} \right] \\
 A_8 &= a_{55} \kappa \left[\frac{4}{3} \sum_{m=1}^N c_{im}^{(1)} W_m \sum_{m=1}^N c_{im}^{(2)} W_m + \frac{3}{\chi_i} U_i^2 + \frac{11}{3\chi_i} \left(\sum_{m=1}^N c_{im}^{(1)} W_m \right)^2 \right. \\
 &\quad \left. - \frac{2}{\chi_i} U_i \sum_{m=1}^N c_{im}^{(2)} U_m - 4 \sum_{m=1}^N c_{im}^{(1)} U_m \sum_{m=1}^N c_{im}^{(2)} U_m - \frac{3}{\chi_i} \left(\sum_{m=1}^N c_{im}^{(1)} U_m \right)^2 \right] \\
 A_9 &= a_{66} \kappa^2 \left[\frac{6}{\chi_i} \left(\sum_{m=1}^N c_{im}^{(1)} U_m \right)^3 - \frac{6}{\chi_i} U_i^3 - \frac{3}{\chi_i} U_i^2 \sum_{m=1}^N c_{im}^{(1)} U_m \right. \\
 &\quad \left. + \frac{3}{\chi_i} U_i^2 \sum_{m=1}^N c_{im}^{(2)} U_m + \frac{3}{\chi_i} U_i \left(\sum_{m=1}^N c_{im}^{(1)} U_m \right)^2 \right. \\
 &\quad \left. + \frac{1}{\chi_i} U_i \left(\sum_{m=1}^N c_{im}^{(1)} W_m \right)^2 - \frac{8}{3\chi_i} U_i \sum_{m=1}^N c_{im}^{(1)} W_m \sum_{m=1}^N c_{im}^{(2)} W_m \right. \\
 &\quad \left. + \frac{8}{\chi_i} U_i \sum_{m=1}^N c_{im}^{(1)} U_m \sum_{m=1}^N c_{im}^{(2)} U_m - \frac{10}{3} \left(\sum_{m=1}^N c_{im}^{(1)} W_m \right)^2 \sum_{m=1}^N c_{im}^{(2)} U_m \right. \\
 &\quad \left. - \frac{10}{3} \frac{1}{\chi_i} \sum_{m=1}^N c_{im}^{(1)} U_m \left(\sum_{m=1}^N c_{im}^{(1)} W_m \right)^2 \right. \\
 &\quad \left. - \frac{20}{3} \sum_{m=1}^N c_{im}^{(1)} U_m \sum_{m=1}^N c_{im}^{(1)} W_m \sum_{m=1}^N c_{im}^{(2)} W_m \right. \\
 &\quad \left. + 10 \left(\sum_{m=1}^N c_{im}^{(1)} U_m \right)^2 \sum_{m=1}^N c_{im}^{(2)} U_m \right]
 \end{aligned}$$

$$\begin{aligned}
 A_{10} &= a_{55}\kappa \left[\frac{2}{\chi_i} \sum_{m=1}^N c_{im}^{(1)} U_m \sum_{m=1}^N c_{im}^{(1)} W_m + \frac{4}{3\chi_i} U_i \sum_{m=1}^N c_{im}^{(2)} W_m \right. \\
 &\quad \left. + \frac{8}{3} \sum_{m=1}^N c_{im}^{(1)} W_m \sum_{m=1}^N c_{im}^{(2)} U_m + \frac{8}{3} \sum_{m=1}^N c_{im}^{(1)} U_m \sum_{m=1}^N c_{im}^{(2)} W_m \right] \\
 A_{11} &= a_{66}\kappa^2 \left[\frac{1}{\chi_i^3} U_i^2 \sum_{m=1}^N c_{im}^{(1)} W_m - \frac{2}{\chi_i^2} U_i \sum_{m=1}^N c_{im}^{(1)} U_m \sum_{m=1}^N c_{im}^{(1)} W_m \right. \\
 &\quad - \frac{1}{\chi_i} U_i^2 \sum_{m=1}^N c_{im}^{(2)} W_m + \frac{2}{3\chi_i} \left(\sum_{m=1}^N c_{im}^{(1)} W_m \right)^3 - \frac{6}{\chi_i} \sum_{m=1}^N c_{im}^{(1)} W_m \left(\sum_{m=1}^N c_{im}^{(1)} U_m \right)^2 \\
 &\quad - \frac{8}{3\chi_i} U_i \sum_{m=1}^N c_{im}^{(1)} W_m \sum_{m=1}^N c_{im}^{(2)} U_m - \frac{20}{3} \sum_{m=1}^N c_{im}^{(1)} U_m \sum_{m=1}^N c_{im}^{(1)} W_m \sum_{m=1}^N c_{im}^{(2)} U_m \\
 &\quad - \frac{10}{3} \left(\sum_{m=1}^N c_{im}^{(1)} U_m \right)^2 \sum_{m=1}^N c_{im}^{(2)} W_m - \frac{8}{3\chi_i} U_i \sum_{m=1}^N c_{im}^{(1)} U_m \sum_{m=1}^N c_{im}^{(2)} W_m \\
 &\quad \left. + 2 \left(\sum_{m=1}^N c_{im}^{(1)} W_m \right)^2 \sum_{m=1}^N c_{im}^{(2)} W_m \right] \tag{57}
 \end{aligned}$$

where

$$\begin{cases} b_1 = \sum_{i=1}^{N_L} \int_{h_i}^{h_{i+1}} \left(\frac{V_{(i)}^2 \varepsilon_0 \varepsilon_r(i)}{C_0 h^3} \right) dz \\ a_{55} = \frac{6a_1}{\eta^7} \\ a_{66} = \frac{6a_1}{\eta^8} \end{cases} \tag{58}$$

Appendix 2

$$\begin{aligned}
 \mathbf{K}_{NL} &= \begin{bmatrix} \mathbf{K}_{NL}(11) & \mathbf{K}_{NL}(12) \\ & \mathbf{K}_{NL}(21) & \mathbf{K}_{NL}(22) \end{bmatrix} \\
 &= \begin{bmatrix} A & \dots & B & E & \dots & F \\ \vdots & \ddots & \vdots & \vdots & \ddots & \vdots \\ C & \dots & D & G & \dots & H \\ I & \dots & J & M & \dots & N \\ \vdots & \ddots & \vdots & \vdots & \ddots & \vdots \\ K & \dots & L & O & \dots & P \end{bmatrix} \tag{59}
 \end{aligned}$$

where

$$\begin{aligned}
 A &= a_{55}\kappa \left(\frac{3}{\chi_i^3} U_1 \right) - \frac{2a_{55}\kappa}{\chi_i} \sum_{m=1}^N c_{1m}^{(2)} U_m \\
 &\quad - 4a_{55}\kappa \left(\sum_{m=1}^N c_{1m}^{(2)} U_m \right) c_{11}^{(1)} - \frac{3a_{55}\kappa}{\chi_i} \left(\sum_{m=1}^N c_{1m}^{(1)} U_m \right) c_{11}^{(1)} \\
 &\quad - a_{66}\kappa^2 \left(\frac{6}{\chi_i^4} U_1^2 \right) + \frac{6a_{66}\kappa^2}{\chi_i} \left(\sum_{m=1}^N c_{1m}^{(1)} U_m \right)^2 c_{11}^{(1)} \\
 &\quad - \frac{3a_{66}\kappa^2}{\chi_i^3} (U_1^2) c_{11}^{(1)} + \frac{3a_{66}\kappa^2}{\chi_i^2} U_1 \sum_{m=1}^N c_{1m}^{(2)} U_m \\
 &\quad + \frac{3a_{66}\kappa^2}{\chi_i^2} U_1 \left(\sum_{m=1}^N c_{1m}^{(1)} U_m \right) c_{11}^{(1)} + \frac{8a_{66}\kappa^2}{\chi_i} U_1 \left(\sum_{m=1}^N c_{1m}^{(2)} U_m \right) c_{11}^{(1)} \\
 &\quad - \frac{20a_{66}\kappa^2}{3} \left(\sum_{m=1}^N c_{1m}^{(1)} W_m \right) \left(\sum_{m=1}^N c_{1m}^{(2)} W_m \right) c_{11}^{(1)} \\
 &\quad + 10a_{66}\kappa^2 \left(\sum_{m=1}^N c_{1m}^{(1)} U_m \right) \left(\sum_{m=1}^N c_{1m}^{(2)} U_m \right) c_{11}^{(1)} \\
 &\quad - a_{33} \left[\frac{1}{\chi_i^3} U_1 - \frac{2}{\chi_i} \sum_{m=1}^N c_{1m}^{(2)} U_m - \frac{1}{\chi_i} \left(\sum_{m=1}^N c_{1m}^{(1)} U_m \right) c_{11}^{(1)} \right] \\
 &\quad - a_{44} \left[\frac{1}{\chi_i^3} U_1 \sum_{m=1}^N c_{1m}^{(1)} U_m - \frac{1}{\chi_i^2} U_1 \sum_{m=1}^N c_{1m}^{(2)} U_m \right. \\
 &\quad \left. - \frac{1}{\chi_i^2} \left(\sum_{m=1}^N c_{1m}^{(1)} U_m \right)^2 + \frac{1}{\chi_i^2} \left(\sum_{m=1}^N c_{1m}^{(1)} W_m \right)^2 \right] \tag{60}
 \end{aligned}$$

$$\begin{aligned}
 B &= a_{55}\kappa \left(\frac{3}{\chi_i^3} U_1 \right) - \frac{2a_{55}\kappa}{\chi_i} \sum_{m=1}^N c_{1m}^{(2)} U_m - 4a_{55}\kappa \left(\sum_{m=1}^N c_{1m}^{(2)} U_m \right) c_{1N}^{(1)} \\
 &\quad - \frac{3a_{55}\kappa}{\chi_i} \left(\sum_{m=1}^N c_{1m}^{(1)} U_m \right) c_{1N}^{(1)} - a_{66}\kappa^2 \left(\frac{6}{\chi_i^4} U_1^2 \right) \\
 &\quad + \frac{6a_{66}\kappa^2}{\chi_i} \left(\sum_{m=1}^N c_{1m}^{(1)} U_m \right)^2 c_{1N}^{(1)} - \frac{3a_{66}\kappa^2}{\chi_i^3} (U_1^2) c_{1N}^{(1)} + \frac{3a_{66}\kappa^2}{\chi_i^2} \\
 &\quad U_1 \sum_{m=1}^N c_{1m}^{(2)} U_m + \frac{3a_{66}\kappa^2}{\chi_i^2} U_1 \left(\sum_{m=1}^N c_{1m}^{(1)} U_m \right) c_{1N}^{(1)} \\
 &\quad + \frac{8a_{66}\kappa^2}{\chi_i} U_1 \left(\sum_{m=1}^N c_{1m}^{(2)} U_m \right) c_{1N}^{(1)} - \frac{20a_{66}\kappa^2}{3} \left(\sum_{m=1}^N c_{1m}^{(1)} W_m \right) \\
 &\quad \left(\sum_{m=1}^N c_{1m}^{(2)} W_m \right) c_{1N}^{(1)} + 10a_{66}\kappa^2 \left(\sum_{m=1}^N c_{1m}^{(1)} U_m \right) \left(\sum_{m=1}^N c_{1m}^{(2)} U_m \right) c_{1N}^{(1)} \\
 &\quad - a_{33} \left[\frac{1}{\chi_i^3} U_1 - \frac{2}{\chi_i} \sum_{m=1}^N c_{1m}^{(2)} U_m - \frac{1}{\chi_i} \left(\sum_{m=1}^N c_{1m}^{(1)} U_m \right) c_{1N}^{(1)} \right] \\
 &\quad - a_{44} \left[\frac{1}{\chi_i^3} U_1 \sum_{m=1}^N c_{1m}^{(1)} U_m - \frac{1}{\chi_i^2} U_1 \sum_{m=1}^N c_{1m}^{(2)} U_m \right. \\
 &\quad \left. - \frac{1}{\chi_i^2} \left(\sum_{m=1}^N c_{1m}^{(1)} U_m \right)^2 + \frac{1}{\chi_i^2} \left(\sum_{m=1}^N c_{1m}^{(1)} W_m \right)^2 \right] \tag{61}
 \end{aligned}$$

$$\begin{aligned}
P = & \frac{8a_{55}\kappa}{3} \left(\sum_{m=1}^N c_{Nm}^{(2)} U_m \right) c_{NN}^{(1)} + \frac{a_{66}\kappa^2}{\chi_i^3} U_N^2 c_{NN}^{(1)} \\
& - \frac{6a_{66}\kappa^2}{\chi_i} \left(\sum_{m=1}^N c_{Nm}^{(1)} U_m \right)^2 c_{NN}^{(1)} - \frac{8a_{66}\kappa^2}{3\chi_i} U_N \left(\sum_{m=1}^N c_{Nm}^{(2)} U_m \right) c_{NN}^{(1)} \\
& + \frac{2a_{66}\kappa^2}{3\chi_i} \left(\sum_{m=1}^N c_{Nm}^{(1)} W_m \right)^2 c_{NN}^{(1)} \\
& + 2a_{66}\kappa^2 \left(\sum_{m=1}^N c_{Nm}^{(1)} W_m \right) \left(\sum_{m=1}^N c_{Nm}^{(2)} W_m \right) c_{NN}^{(1)}
\end{aligned} \quad (75)$$

References

- Zhang, J., Chen, H., Li, D.: Pinnacle elimination and stability analyses in nonlinear oscillation of soft dielectric elastomer slide actuators. *Nonlinear Dyn.* **94**, 1907–1920 (2018)
- Luo, K., Tian, Q., Hu, H.: Dynamic modeling, simulation and design of smart membrane systems driven by soft actuators of multilayer dielectric elastomers. *Nonlinear Dyn.* **102**, 1463–1483 (2020)
- York, A., Dunn, J., Seelecke, S.: Systematic approach to development of pressure sensors using dielectric electro-active polymer membranes. *Smart Mater. Struct.* **22**, 094015 (2013)
- Khalid, M.A.U., Ali, M., Soomro, A.M., Kim, S.W., Kim, H.B., Lee, B.G., Choi, K.H.: A highly sensitive biodegradable pressure sensor based on nanofibrous dielectric. *Sens. Actuat. A: Phys.* **294**, 140–147 (2019)
- Lai, Z., Thomson, G., Yurchenko, D., Val, D.V., Rodgers, E.: On energy harvesting from a vibro-impact oscillator with dielectric membranes. *Mech. Syst. Signal.* **107**, 105–121 (2018)
- Lai, Z., Wang, S., Zhu, L., Zhang, G., Wang, J., Yang, K., Yurchenko, D.: A hybrid piezo-dielectric wind energy harvester for high-performance vortex-induced vibration energy harvesting. *Mech. Syst. Signal.* **150**, 107212 (2021)
- Cao, C., Gao, X., Conn, A.T.: A magnetically coupled dielectric elastomer pump for soft robotics. *Adv. Mater. Technol.* **4**, 1900128 (2019)
- Youn, J.H., Jeong, S.M., Hwang, G., Kim, H., Hyeon, K., Park, J., Kyung, K.U.: Dielectric elastomer actuator for soft robotics applications and challenges. *Appl. Sci.* **10**, 640 (2020)
- Arifeen, W.U., Kim, M., Choi, J., Yoo, K., Kurniawan, R., Ko, T.J.: Optimization of porosity and tensile strength of electrospun polyacrylonitrile nanofibrous membranes. *Mater. Chem. Phys.* **229**, 310–318 (2019)
- Wang, J., Chen, B., Cheng, X., Li, Y., Ding, M., You, J.: Hierarchically porous membranes with multiple channels: fabrications in PVDF/PMMA/PLLA blend and enhanced separation performance. *J. Membr. Sci.* **643**, 120065 (2022)
- Li, Q., Liu, Y., Liu, Y., Ji, Y., Cui, Z., Yan, F., Li, J., Younas, M., He, B.: Mg²⁺/Li⁺ separation by electric field assisted nanofiltration: the impacts of membrane pore structure, electric property and other process parameters. *J. Membr. Sci.* **662**, 120982 (2022)
- Wang, H., Zhang, H., Cheng, X.W., Liu, L., Chang, S., Mu, X., Ge, Y.: Microstructure and mechanical properties of GNP's and in-situ TiB hybrid reinforced Ti–6Al–4V matrix composites with 3D network architecture. *Mater. Sci. Eng. A.* **854**, 143536 (2022)
- Sun, R., Li, L., Feng, C., Kitipornchai, S., Yang, J.: Tensile behavior of polymer nanocomposite reinforced with graphene containing defects. *Eur. Polym. J.* **98**, 475–482 (2018)
- Mahmun, A., Kirtania, S.: Evaluation of elastic properties of graphene nanoplatelet/epoxy nanocomposites. *Mater. Today Proc.* **44**, 1531–1535 (2021)
- Mergen, Ö.B., Umud, E., Arda, E., Kara, S.A.: comparative study on the AC/DC conductivity, dielectric and optical properties of polystyrene/graphene nanoplatelets (PS/GNP) and multi-walled carbon nanotube (PS/MWCNT) nanocomposites. *Polym. Test.* **90**, 106682 (2020)
- Liu, J., Zhang, M., Guan, L., Wang, C., Shi, L., Jin, Y., Han, C., Wang, J., Han, Z.: Preparation of BT/GNP/PS/PVDF composites with controllable phase structure and dielectric properties. *Polym. Test.* **100**, 107236 (2021)
- Xia, X., Wang, Y., Zhong, Z., Weng, G.J.: A frequency-dependent theory of electrical conductivity and dielectric permittivity for graphene-polymer nanocomposites. *Carbon* **111**, 221–230 (2017)
- Feng, C., Kitipornchai, S., Yang, J.: Nonlinear free vibration of functionally graded polymer composite beams reinforced with graphene nanoplatelets (GPLs). *Eng. Struct.* **140**, 110–119 (2017)
- Feng, C., Kitipornchai, S., Yang, J.: Nonlinear bending of polymer nanocomposite beams reinforced with non-uniformly distributed graphene platelets (GPLs). *Compos. B Eng.* **110**, 132–140 (2017)
- Shen, H.S., Lin, F., Xiang, Y.: Nonlinear vibration of functionally graded graphene-reinforced composite laminated beams resting on elastic foundations in thermal environments. *Nonlinear Dyn.* **90**, 899–914 (2017)
- Song, M., Gong, Y., Yang, J., Zhu, W., Kitipornchai, S.: Free vibration and buckling analyses of edge-cracked functionally graded multilayer graphene nanoplatelet-reinforced composite beams resting on an elastic foundation. *J. Sound Vib.* **458**, 89–108 (2019)
- Song, M., Gong, Y., Yang, J., Zhu, W., Kitipornchai, S.: Nonlinear free vibration of cracked functionally graded graphene platelet-reinforced nanocomposite beams in thermal environments. *J. Sound Vib.* **468**, 115115 (2020)
- Li, X., Song, M., Yang, J., Kitipornchai, S.: Primary and secondary resonances of functionally graded graphene platelet-reinforced nanocomposite beams. *Nonlinear Dyn.* **95**, 1807–1826 (2019)
- Song, M., Zhou, L., Karunasena, W., Yang, J., Kitipornchai, S.: Nonlinear dynamic instability of edge-cracked functionally graded graphene-reinforced composite beams. *Nonlinear Dyn.* **109**, 2423–2441 (2022)
- Wang, Y., Feng, C., Yang, J., Zhou, D., Wang, S.: Nonlinear vibration of FG-GPLRC dielectric plate with active tuning using differential quadrature method. *Comput. Methods Appl. Mech. Eng.* **379**, 113761 (2021)
- Song, M., Li, X., Kitipornchai, S., Bi, Q., Yang, J.: Low-velocity impact response of geometrically nonlinear

- functionally graded graphene platelet-reinforced nanocomposite plates. *Nonlinear Dyn.* **95**, 2333–2352 (2019)
27. Dong, Y., Li, Y., Li, X., Yang, J.: Active control of dynamic behaviors of graded graphene reinforced cylindrical shells with piezoelectric actuator/sensor layers. *Appl. Math. Model.* **82**, 252–270 (2020)
 28. Ye, C., Wang, Y.Q.: Nonlinear forced vibration of functionally graded graphene platelet-reinforced metal foam cylindrical shells: internal resonances. *Nonlinear Dyn.* **104**, 2051–2069 (2021)
 29. Wang, Y., Feng, C., Zhao, Z., Lu, F., Yang, J.: Torsional buckling of graphene platelets (GPLs) reinforced functionally graded cylindrical shell with cutout. *Compos. Struct.* **197**, 72–79 (2018)
 30. Ni, Z., Fan, Y., Hang, Z., Yang, J., Wang, Y., Feng, C.: Numerical investigation on nonlinear vibration of FG-GNPRC dielectric membrane with internal pores. *Eng. Struct.* **284**, 115928 (2023)
 31. Weng, G.J.: A dynamical theory for the Mori–Tanaka and Ponte Castañeda–Willis estimates. *Mech. Mater.* **42**, 886–893 (2010)
 32. Su, Y., Li, J.J., Weng, G.J.: Theory of thermal conductivity of graphene-polymer nanocomposites with interfacial Kapitza resistance and graphene-graphene contact resistance. *Carbon* **137**, 222–233 (2018)
 33. Wang, J., Li, J.J., Weng, G.J., Su, Y.: The effects of temperature and alignment state of nanofillers on the thermal conductivity of both metal and nonmetal based graphene nanocomposites. *Acta Mater.* **185**, 461–473 (2020)
 34. Hashemi, R., Weng, G.J.: A theoretical treatment of graphene nanocomposites with percolation threshold, tunneling-assisted conductivity and microcapacitor effect in AC and DC electrical settings. *Carbon* **96**, 474–490 (2016)
 35. Wang, Y., Shan, J.W., Weng, G.J.: Percolation threshold and electrical conductivity of graphene-based nanocomposites with filler agglomeration and interfacial tunneling. *J. Appl. Phys.* **118**, 065101 (2015)
 36. Wang, Y., Weng, G.J., Meguid, S.A., Hamouda, A.M.: A continuum model with a percolation threshold and tunneling-assisted interfacial conductivity for carbon nanotube-based nanocomposites. *J. Appl. Phys.* **115**, 193706 (2014)
 37. Dyre, J.C.: A simple model of ac hopping conductivity in disordered solids. *Phys. Lett.* **108**, 457–461 (1985)
 38. Ji, D., Xiao, C., Chen, K., Zhou, F., Gao, Y., Zhang, T., Ling, H.: Solvent-free green fabrication of PVDF hollow fiber MF membranes with controlled pore structure via melt-spinning and stretching. *J. Membr. Sci.* **621**, 118953 (2021)
 39. Odegard, G., Gates, T., Wise, K., Park, C., Siochi, E.: Constitutive modeling of nanotube-reinforced polymer composites. *Compos. Sci. Technol.* **63**, 1671–1687 (2003)
 40. Feng, C., Wang, Y., Kitipornchai, S., Yang, J.: Effects of reorientation of graphene platelets (GPLs) on Young's Modulus of polymer nanocomposites under uni-axial stretching. *Polymers* **9**, 532 (2017)
 41. Li, B., Chen, H., Qiang, J., Hu, S., Zhu, Z., Wang, Y.: Effect of mechanical pre-stretch on the stabilization of dielectric elastomer actuation. *J. Phys. D: Appl. Phys.* **44**, 155301 (2011)
 42. Gonçalves, P.B., Soares, R.M., Pamplona, D.: Nonlinear vibrations of a radially stretched circular hyperelastic membrane. *J. Sound Vib.* **327**, 231–248 (2009)
 43. Treloar, L.R.G.: *The Physics of Rubber Elasticity*. Oxford University Press, New York (1958)
 44. Selvadurai, A.P.S.: Deflections of a rubber membrane. *J. Mech. Phys. Solids.* **54**, 1093–1119 (2006)
 45. Gent, A.N.: Elastic instabilities in rubber. *Int. J. Non-Linear Mech.* **40**, 165–175 (2005)
 46. Pamplona, D.C., Gonçalves, P.B., Lopes, S.R.X.: Finite deformations of cylindrical membrane under internal pressure. *Int. J. Mech. Sci.* **48**, 683–696 (2006)
 47. Suo, Z.: Theory of dielectric elastomers. *Acta Mech. Solida Sin.* **23**, 549–578 (2010)
 48. Ni, Z., Zhu, F., Fan, Y., Yang, J., Hang, Z., Feng, C., Yang, J.: Numerical study on nonlinear vibration of FG-GNPRC circular membrane with dielectric properties. *Mech. Adv. Mater. Struct.* (2023). <https://doi.org/10.1080/15376494.2023.2184005>
 49. Mrabet, K., Zaouali, E., Najjar, F.: Internal resonance and nonlinear dynamics of a dielectric elastomer circular membrane. *Int. J. Solids Struct.* **236–237**, 111338 (2022)
 50. Ni, Z., Fan, Y., Hang, Z., Zhu, F., Wang, Y., Feng, C., Yang, J.: Damped vibration analysis of graphene nanoplatelet reinforced dielectric membrane using Taylor series expansion and differential quadrature methods. *Thin-Walled Struct.* **184**, 110493 (2023)
 51. Zhu, F., Feng, C., Wang, Y., Qian, Q., Hang, Z., Yang, J., Wang, S.: Damped nonlinear dynamics of FG-GPLRC dielectric beam with active tuning using DQ and IHB methods. *Int. J. Struct. Stab. Dyn.* **23**, 2350079 (2022)
 52. He, F., Lau, S., Chan, H.L., Fan, J.: High dielectric permittivity and low percolation threshold in nanocomposites based on poly(vinylidene fluoride) and exfoliated graphite nanoplates. *Adv. Mater.* **21**, 710–715 (2009)

Publisher's Note Springer Nature remains neutral with regard to jurisdictional claims in published maps and institutional affiliations.

Springer Nature or its licensor (e.g. a society or other partner) holds exclusive rights to this article under a publishing agreement with the author(s) or other rightsholder(s); author self-archiving of the accepted manuscript version of this article is solely governed by the terms of such publishing agreement and applicable law.